POLITECNICO DI TORINO

MASTER's Degree in ELECTRICAL ENGINEERING

MASTER's Degree Thesis

REALIZATION OF A SYSTEM FOR CONTROLLING AND MEASURING THE PERFORMANCE OF A MAGNETIC GEARBOX

Supervisors

Prof. MAURIZIO REPETTO

Dr. LUCA DIMAURO

PAOLO SQUILLARI

Candidate

GABRIELE PIRRA

NOVEMBER 2021

Summary

Magnetic Gears have been proposed for motion transmission since years 80s of last century. Their main characteristic is the torque transfer between two coaxial permanent magnets rotors through the interaction with a set of ferromagnetic poles but without mechanical contact. From the kinematic point of view their working is similar to the one of epicyclic gearing or planetary gearing and they can transmit torque with a constant gear ratio determined by the number of permanent magnet pole pairs and of modulating iron poles. A test bench for measuring magnetic gear performance has been devised and realised. Magnetic gears have been equipped with sensors coils to monitor the magnetic flux inside the structure and to compare it with simulation predictions. Details about the test bench, its drives and controls and preliminary results obtained by tests are presented and discussed.

Acknowledgements

Before proceeding with the discussion, i would like to dedicate a few lines to all those who have been close to me in these years of personal and professional growth.
I would like to express my gratitude to my primary supervisor, Maurizio Repetto, who guided me throughout this project with his encouragement and support.
Thanks to my co-supervisors Luca Dimauro and Paolo Squillari, who helped me to realize this project with their patience and availability.
A special thanks to my father, my mother and all my family who have always believed in me giving me strength even in the most difficult moments.

Table of Contents

List of Tables

List of Figures

Chapter 1

Introduction

1.1 Magnetic Gear

Mechanical gearboxes are widely used to convert and adapt the output torque and speed from a motor to the requirements of the load. It is usually more cost and weight effective to employ a high-speed motor together with a gearbox to transfer the power.
However, although high system torque densities can be achieved, gearboxes usually require lubrication and cooling and have problems related to noise, vibration and reliability.
Magnetic gears offer several potential advantages, such as:

- Reduced acoustic noise and vibration.
- Reduced maintenance and improved reliability.
- Precise peak torque transmission capability and inherent overload protection.
- Physical isolation between input and output shafts.

They are used in several renewable energy applications, increasing the speed of wind energy, ocean energy, and flywheel energy storage in order to match the specification of the electromagnetic generator.

There are different types of magnetic gears, in this thesis the one proposed by Atallah [1] is studied and analyzed. This solution have a transmitted torque density capability which is comparable with that of two and three-stage epicyclic gearboxes.

1.1.1 History

A review on magnetic gears is proposed in [2] and here reported.
The first idea of a magnetic gearbox dates back to the beginning of the 20^{th} century. In 1901 Armstrong patented a power-transmitting device by means of magnetic force, though the magnetism is produced by coils instead of permanent magnets (PMs) [3]. Forty years later, H.T.Faus invented the first magnetic gear (MG) which adopted pure PMs (Figure 1.1) [4].

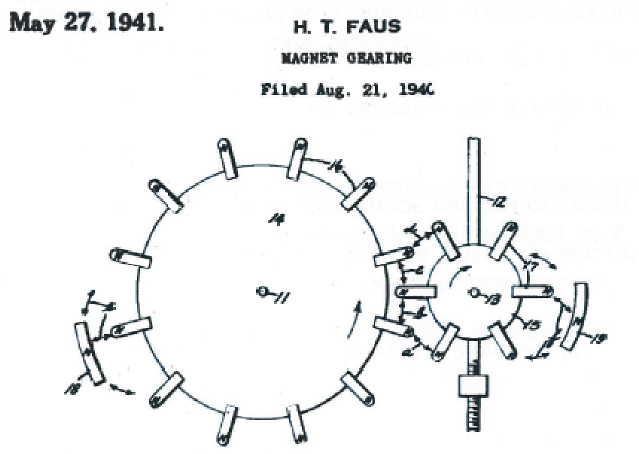

Figure 1.1: Scheme of the H.T.Faus magnetic gear [5].

In 1968, a patent concerning a coaxial MG was proposed by Martin [6].
Many different Magnetic Gears topologies appeared at that period, however, the torque density was quite poor due to the low performance and utilization of ferrite permanent magnets. Furthermore, as the structure of the MG derived directly from the equivalent mechanical gear topology, where slots and teeth of iron core were replaced by permanent magnets, the torque density was weak because only one magnet on each disk contributed to the transmission of the force.
With the advent of rare-earth high performance magnets and the born of the neodymium (NdFeB) permanent magnet in 1980s, new and more performing MGs have been developed.
In 2001, Atallah [1] presents the coaxial magnetic gear (Figure 1.2). This structure is different from those proposed previously, indeed all the permanent magnets are used simultaneously and contribute to torque transmission. Consequently, a high torque density can be reach ($50 \div 150kNm/m^3$).

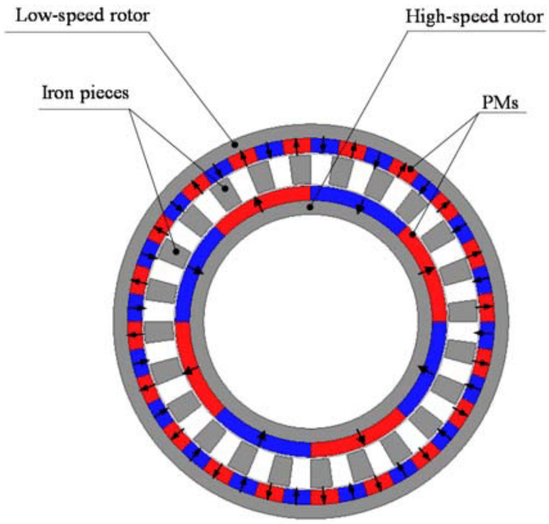

Figure 1.2: Magnetic gear proposed by Atallah [7].

In 2008, C.Huang proposed a magnetic planetary gear (Figure 1.3). This solution is a copy of the mechanical planetary gear but the teeth are replaced by magnets. Despite having a good reliability, it is not widely used because the torque density seems to be weak in comparison of its mechanical counterpart and presents also an high cogging torque.

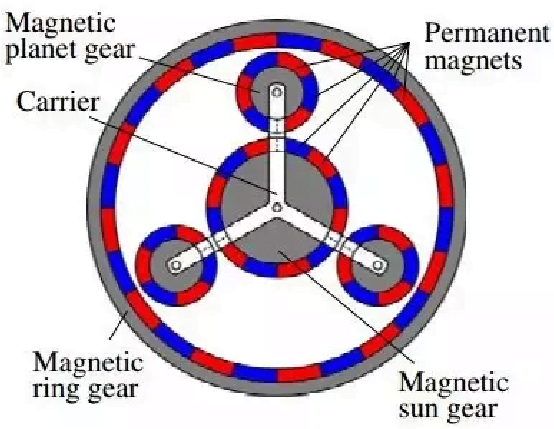

Figure 1.3: Magnetic planetary gear proposed by C.Huang [8].

1.1.2 Principle of operation

In figure 1.4 is shown a typical coaxial magnetic gear. It is composed of an inner and an outer rotor. Each rotor as a different number of permanent magnet pole pieces. Between the two rotors there are a number of ferromagnetic pole pieces. The inner rotor is the high speed rotor while the outer rotor is the low speed one. The ferromagnetic pole pieces are fixed.

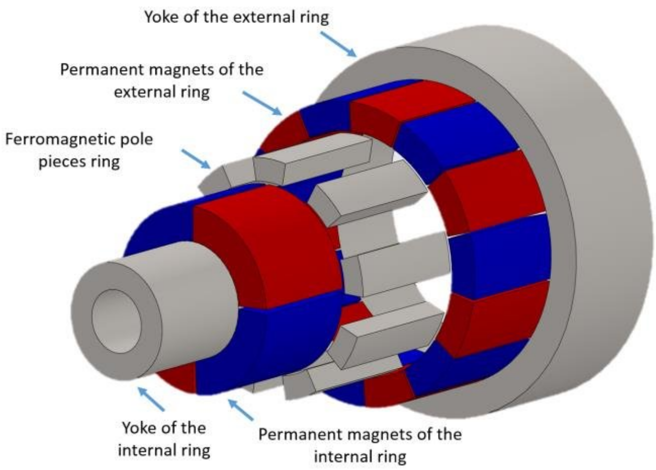

Figure 1.4: Magnetic gear by Atallah (3D figure) [9].

The ferromagnetic pole pieces (middle rotor) modulate the magnetic fields produced by inner and outer rotors and create space harmonics in the air gaps. The modulated magnetic fields via the steel poles interact with the magnetic field on the other side to transmit the torque.

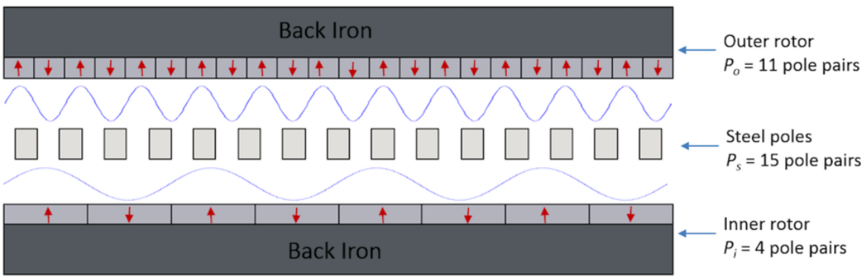

Figure 1.5: Scheme of the components interaction in magnetic gear [5].

The figure 1.5 represent an example of a typical configuration of magnetic gears. The 4 pole pairs on the inner rotor produce the magnetic field with a dominant 4th harmonic. This field is then modulated by 15 steel pole pairs to generate a field with a dominant 11th harmonic. The modulated field interacts with the dominant 11th harmonic field that is produced by the outer rotor to transfer torque. This generates the torque, as the field harmonic component from the outer rotor matches with the harmonic component created by the modulated inner rotor field.

The flux density distribution at a radial distance r produced by either permanent magnet rotor can be written in the following form:

$$B_r(r,\theta) = (\sum_{m=1,3,5...} b_{rm}(r)cos(mp(\theta-\Omega_r t)+mp\theta_0)\cdot(\lambda_{r0}(r)+\sum_{j=1,2,3...} \lambda_{rj}(r)cos(jn_s\theta) \tag{1.1}$$

for the radial component, and

$$B_\theta(r,\theta) = (\sum_{m=1,3,5...} b_{\theta m}(r)sin(mp(\theta-\Omega_r t)+mp\theta_0)\cdot(\lambda_{\theta 0}(r)+\sum_{j=1,2,3...} \lambda_{\theta j}(r)cos(jn_s\theta) \tag{1.2}$$

for the circumferential component, where p is the number of pole-pairs on the permanent magnet rotor, n_s is the number of ferromagnetic pole pieces, and Ω_r is the rotational speed of the permanent magnet rotor. Furthermore, b_{rm}, $b_{\theta m}$ are Fourier coefficients for the radial and circumferential components of the flux density distribution, without the ferromagnetic pole pieces, respectively. Similarly, λ_{rj} and $\lambda_{\theta j}$ are Fourier coefficients for the modulating functions associated with the radial and circumferential components of the flux density distribution resulting from the introduction of the ferromagnetic pole pieces, respectively.
The terms in the first parenthesis of the equations above represents the flux density distribution without ferromagnetic pole pieces(Figure 1.6), while the second parenthesis is the modulating function(Figure 1.7).

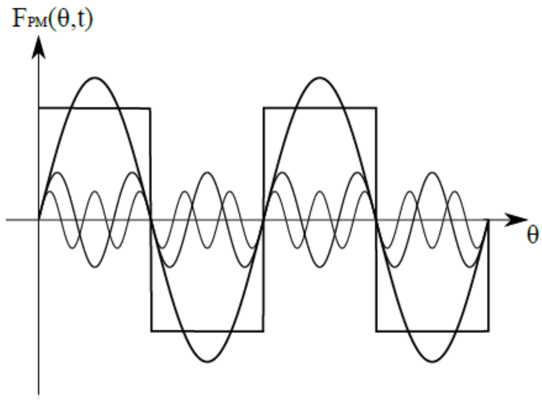

Figure 1.6: MMF waveform produced by the PMs and it's Fourier series representations [10].

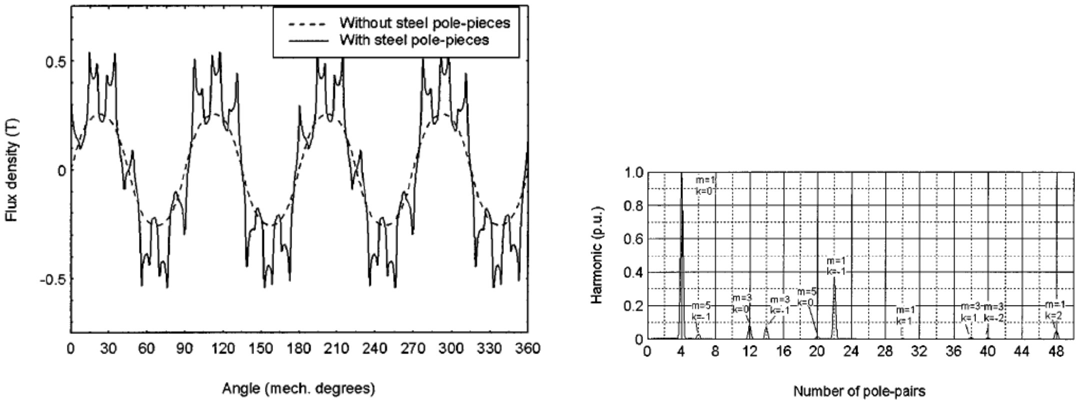

Figure 1.7: Effect of the modulation on the flux density and its spectrum [1].

The number of pole-pairs in the space harmonic flux density distribution produced by either permanent magnet rotor is computed with the following formula:

$$\begin{gathered} p_{m,k} = |mp + kn_s| \\ m = 1,3,5,...,\infty \\ k = 0, \pm 1, \pm 2, \pm 3, ..., \pm\infty \end{gathered} \tag{1.3}$$

while the rotational speed of the flux density space harmonics is given by

$$\Omega_{m,k} = \frac{mp}{mp + kn_s}\Omega_r \tag{1.4}$$

Therefore, to transmit torque at a different rotational speed, the number of pole-pairs of the other permanent magnet rotor must be equal to the number of pole-pairs of a space harmonic for which $k \neq 0$. Since the combination $m = 1$, $k = -1$, results in the highest asynchronous space harmonic, the number of pole-pairs of the other rotor must be equal to $(n_s - p)$. The gear ratio is then given by

$$G_r = \frac{n_s - p}{p} \tag{1.5}$$

Chapter 2

Design and simulation of Magnetic Gear

2.1 Power losses

The procedure for computing magnetic losses in coaxial magnetic gears is well described in [11] and is briefly reported here.
The flux distribution inside the iron parts is computed by means of the finite element method and a model of iron losses taking into account the rotational nature of the flux loci is applied. The results provide indications on the behavior of the power loss for each part of the machine.
First of all a preliminary analysis has been carried out in order to compare the results in terms of magnetic flux distribution for a 3D and a 2D finite element model.
For the 2D modeling the analysis is conducted considering the reference magnetic gear sketched in Figure 2.1.

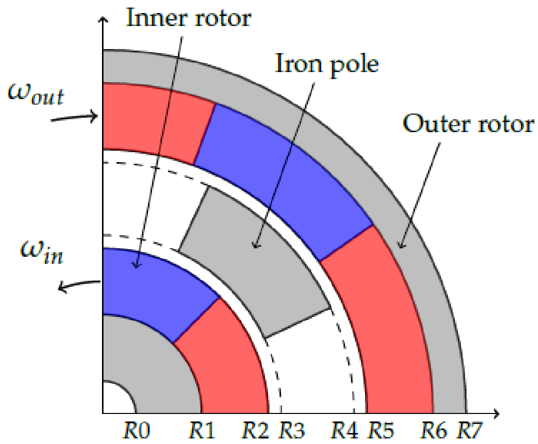

Figure 2.1: Magnetic gear structure for 2D power loss analysis [11].

Parameter	Value
R0	0.02 m
R1	0.04 m
R2	0.05 m
R3	0.052 m
R4	0.062 m
R5	0.064 m
R6	0.074 m
R7	0.09 m
Axial length L	0.1 m
Inner pole pairs P_i	2
Outer pole pairs P_o	11
Iron poles q	13
Gear ratio $\lvert G\rvert = \lvert -P_o/P_i\rvert$	5.5

Table 2.1: List of parameters adopted for 2D Power losses analysis.

The equations applied within the gear domain are the quasi-static Maxwell laws. The formulation adopted for the 3D modeling is standard, based on the magnetic vector potential and the scalar electric potential on the conductive permanent magnet regions, while the scalar magnetic potential is adopted in the current-free regions. An example of magnetic flux density norm and the induced eddy currents of the 3D model is shown in Figure 2.2a: since the machine is not periodic, the whole geometry needs to be modeled. These results computed in different sections of the machine are compared with the ones provided by the 2D model for its three main gear parts.

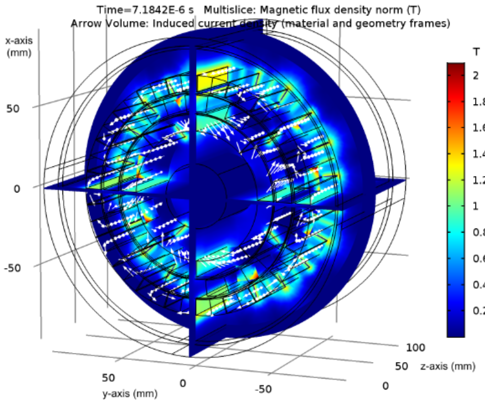

(a) Magnetic flux density norm and eddy current arrow

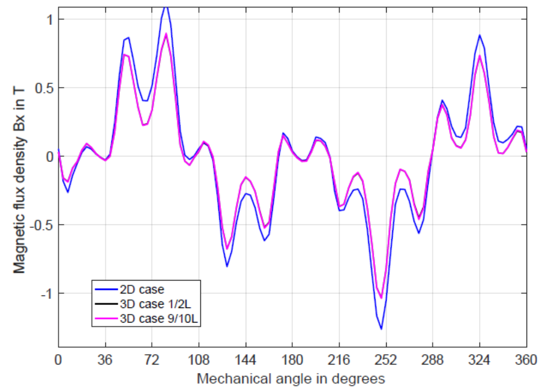

(b) Outer rotor($r = 86.3mm, angle = 0 \div 360°$)

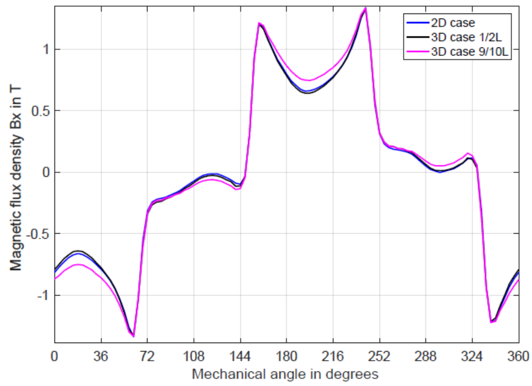

(c) Inner rotor($r = 36.4mm, angle = 0 \div 360°$)

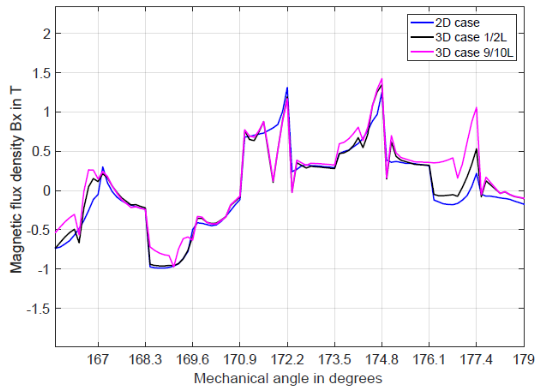

(d) Iron poles ($r = 52.5mm, angle = 167 \div 180°$)

Figure 2.2: Example of magnetic flux density norm and eddy current arrow plot resulting from 3D simulation(a) and Comparison of B_x between 2D and 3D simulations(b-c-d). [11].

Figures 2.2b-2.2c-2.2d show the comparisons of the flux density values along arcs taken inside the inner rotor, outer rotor and iron poles, respectively. In each plot three curves are displayed, one for the 2D case and the others for the 3D case where the flux density is valued along the plan passing through z = L/2 (in the middle of the axial length of the machine) and z = 9L/10.
The comparison shows anyway a good match between 2D and 3D simulations, thus the loss estimation is based on the flux density computed from 2D simulations.

A rational approach to the 2D magnetic losses and their frequency dependence can be pursued in non-oriented steel sheets following the method and the tools based on the statistical theory of loss of Bertotti. This method is based on the concept of loss separation, by which the total loss W is expressed as the sum of the hysteresis W_{hyst}, excess W_{exc}, and classical W_{class} components

$$W = W_{hyst} + W_{exc} + W_{class} \tag{2.1}$$

and the connection with their unidirectional counterpart by an equivalent ellipsoid. Following this approach, the hysteresis loss for a given elliptical flux locus is expressed as:

$$W_{hyst}(J_p, a) \cong W_{hyst}^{(ALT)}(J_p) + W_{hyst}^{(ALT)}(aJ_p)(R_{hyst}(Jp) - 1) \tag{2.2}$$

where

- $R_{hyst} = W_{hyst}^{(ROT)}/W_{hyst}^{(ALT)}$ is the experimental ratio between the hysteresis losses obtained under circular and alternating polarization.
- $J_p = B_p - \mu_0 H_p$ is the peak polarization along the major axis of the ellipse.
- a is the ratio between minor to major axis lengths: If $a = 0$ only alternating loss is present while $a = 1$ means purely rotating loss.

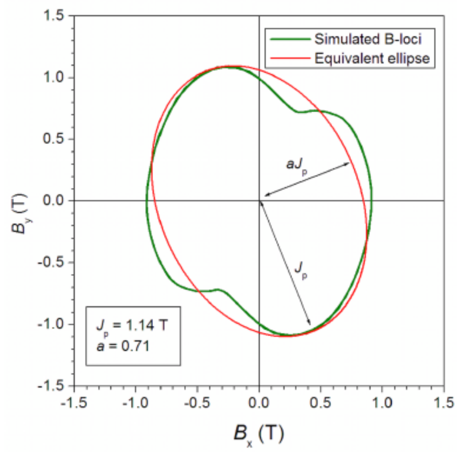

Figure 2.3: B-locus at a given point within the iron pole [11].

The figure 2.4 below represent the global efficiency, permanent magnets efficiency and specific iron loss plots varying the rotational speed. As it can be seen the efficiency decay is practically linear in this speed range and above $w_{in} = 1000rpm$ the highest specific losses are in the iron poles.

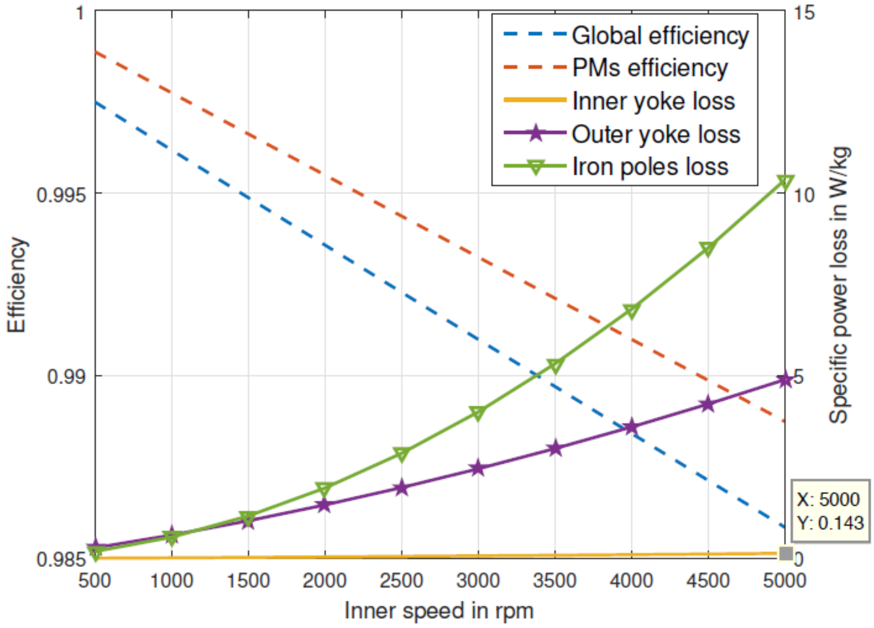

Figure 2.4: Global efficiency, permanent magnets efficiency and specific iron loss plots varying the rotational speed [11].

2.2 Optimisation and design

2.2.1 Optimisation

As shown in figure 2.5 the nomenclature of the mechanical gearbox is adopted to describe the components of the magnetic gear:

- Sun is the name of the inner rotor.
- Carrier is the name of the middle rotor.
- Ring is the name of the outer rotor.

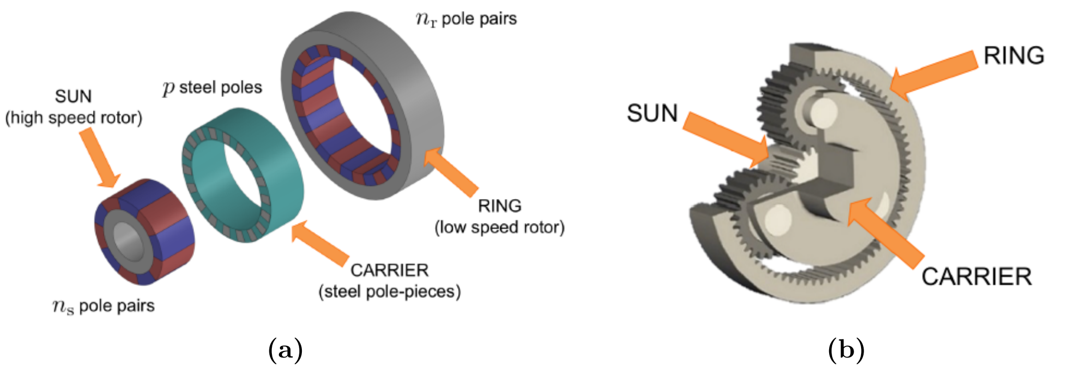

Figure 2.5: Analogy of names between magnetic and mechanical gear [12].

The realization of the magnetic gear under test starts with a multi-objective optimization based on the Pareto front method [12].
The two objectives to be optimized as function of the geometrical parameters used to describe the structure are:

- maximization of torque density.
- minimization of moment of inertia.

The analysis is performed by means of a magneto-static solution of the structure, since eddy currents in conductive parts and losses in ferromagnetic materials, which refers to a dynamic solution, can be neglected. Ferromagnetic saturation is instead taken into account as this effect is of primary importance.
The optimization has been done with using the software FEMM which is based on two-dimensional finite element analysis (in section 2.1 is demonstrated the validity of the two-dimensional analysis compared to the three-dimensional one).
Since the value of the torque depends on the relative position of the three magnetic

parts, a correct analysis would require the evaluation of these values in a significant number of angular position. Under the hypothesis that the steel pole pieces are fixed, each configuration is identified by the angle of the sun (θ_s) and that of the ring (θ_r). Machine periodicity can be exploited to reduce the number of FEM runs, in particular the sun has a periodicity of $\tau_s = 360°/p_s = 72°$ while the ring of $\tau_r = 360°/p_r = 20°$ as it can be seem in figure 2.6. The slope of each curve at constant torque is equal to the gear ratio G. The value of the torque at the points $P1$ is the same of that of the points P^* and P' suitably shifted. Hence, it's possible to reconstruct the overall torque-angles map by analysing the magnetic gear starting from a single configuration of one of the two rotors and rotating the other one within one period.

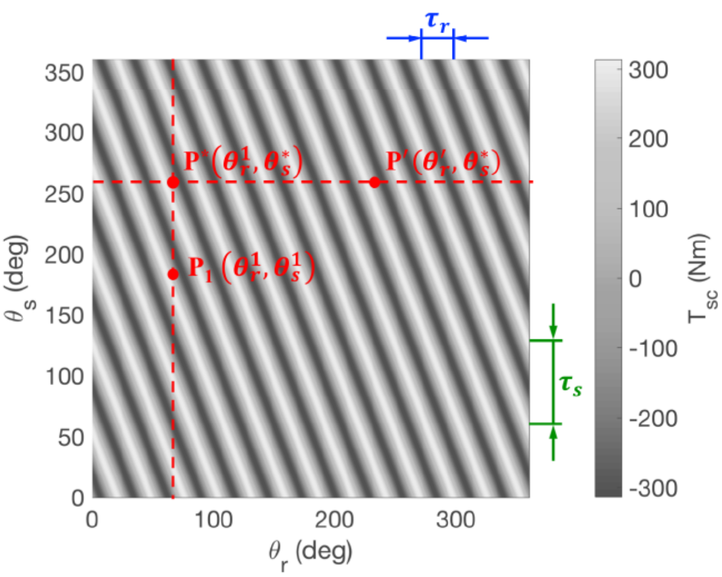

(a)

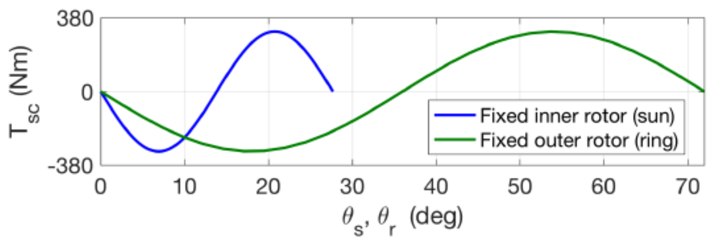

(b)

Figure 2.6: Greyscale map of the sun-carrier torque derived by the simulation of 360 x 360 relative positions of inner and outer rotor (a). Same torque referred to one period τ_r or τ_s while maintaining fixed the position of one of the two rotors (b). [12].

2.2.2 Design

Table 2.2 reported the effective parameters of the magnetic gear under test.

Parameter	Value	Unit
Sun pole pairs	5	
Ring pole pairs	13	
Ferromagnetic pole pieces	18	
Gear ratio	2.6	
Nominal torque on the inner rotor	2.57	Nm
Nominal torque on the outer rotor	6.68	Nm
Nominal torque on the carrier	-9.25	Nm
Weight of active components	0.62	kg
Torque density (related to active components)	3.37	Nm/kg

Table 2.2: Parameters of the magnetic gear under test.

Two perpendicular coils were placed around three ferromagnetic pole pieces out of phase by 120 mechanical degrees in order to reconstruct the waveform of the radial and tangential flux from that of the electromagnetic force measured and compare it with the one obtained form the simulation. Each coil has $N = 18$ number of turns. The section of the radial coil is $A = 0.6581 \cdot 10^{-4}\ m^2$ while the one of the tangential coil is $A = 0.7359 \cdot 10^{-4}\ m^2$.

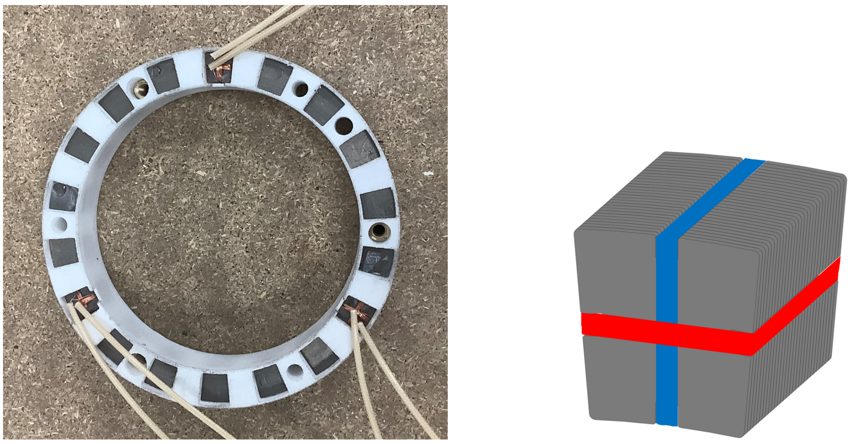

(a) **(b)**

Figure 2.7: Perpendicular coils around ferromagnetic pole pieces on the carrier.

Chapter 3

Hardware

The realization of a system for controlling and measuring the performance of the magnetic gear under test is necessary.
This chapter provides a detailed description of the hardware components of this system: the test bench and the electrical panel.

3.1 Test bench

3.1.1 Structure

The structure of the test bench is needed to support all components that are used to test the MG. The structure is made by metal profiles that have been cut and assembled to achieve the result in figure 3.1c.

(a) (b) (c)

Figure 3.1: Structure of the test bench.

As it can be seen from the figure, a lane has been mounted in the upper floor where the components will be positioned.
The structure has the following dimensions:

Parameter	Value	Unit
Metal profile height	40	mm
Metal profile width	80	mm
Structure height	1	m
Structure width	0.4	m
Structure length	1.3	m

Table 3.1: Dimensions of the test bench structure.

3.1.2 Components

Motors

The test bench requires 2 electric motors connected to the MG shafts, which are the same in this case. it was chosen to use the brushless motors produced by Servotecnica S.p.A. belonging to the SVTM A series.

Figure 3.2: Brushless motors by Servotecnica(SVTM A 03-11.5-107).

The SVTM A series present a type IC 400 construction(the motor is totally enclosed and does not need any kind of additional ventilation) and an IP65 degree of protection. The motor is design with winding in the groove and Neodymium magnets, this ensures high performance with small dimensions, resulting in a sinusoidal electromotive force. For enhanced application safety, a temperature sensor is mounted for each winding so as to prevent damage from overheating and consequently increasing motor service life. For the feedback signal is mounted an incremental encoder with hall effect (2500 ppr).

Parameter	Value	Unit
Frame diameter	115	mm
Motor length	218	mm
Nominal voltage	560	V_{DC}
Continous stall torque	11.5	Nm
Continous stall current	6.85	Arms
Nominal torque	9.3	Nm
Nominal current	5.54	Arms
Nominal speed	2800	rpm
Nominal power	5	kW
Peak torque	30	Nm
Peak current	21	Arms
Torque constant	1.86	Nm/Arms
BEMF constant	107	Vrms/krpm
Rotor inertia	10.8	$kgcm^2$
Thermal protection	PTC	
Mass	9.5	kg

Table 3.2: Brushless motors by Servotecnica (SVTM A 03-11.5-107) parameters [13].

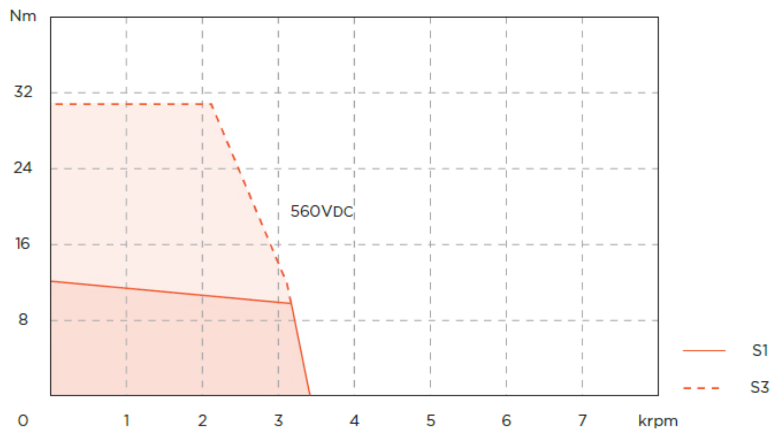

Figure 3.3: Torque limit curve (SVTM A 03-11.5-107) [13].

Magnetic gear

Magnetic gear design was well presented in chapter 1. Figure 3.3 below shows the MG prototype under test.

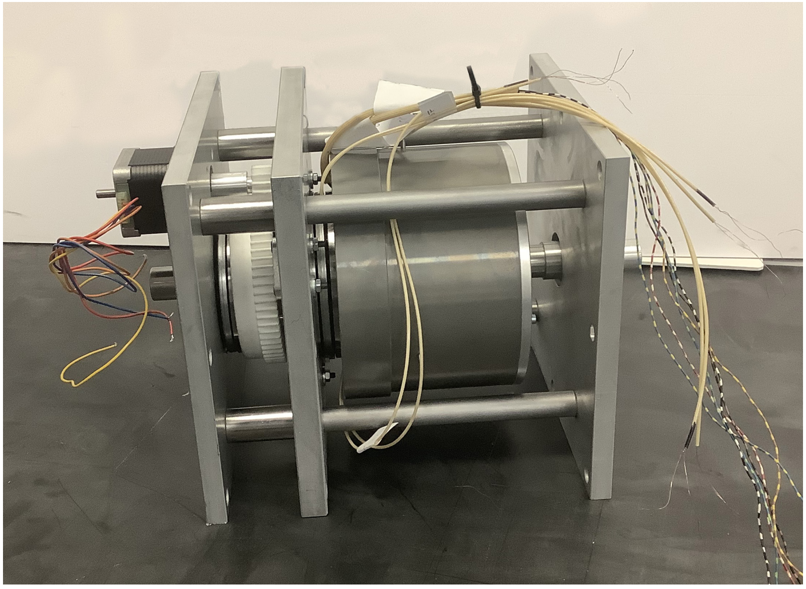

Figure 3.4: Magnetic gear prototype.

To be more comfortable the Table 2.2 with all parameters is repropose in this section.

Parameter	Value	Unit
Sun pole pairs	5	
Ring pole pairs	13	
Ferromagnetic pole pieces	18	
Gear ratio	2.6	
Nominal torque on the inner rotor	2.57	Nm
Nominal torque on the outer rotor	6.68	Nm
Nominal torque on the carrier	-9.25	Nm
Weight of active components	0.62	kg
Torque density (related to active components)	3.37	Nm/kg

Table 3.3: Parameters of the magnetic gear under test.

Torque transducers

Two torque transducers are used to measure the torque transmitted by the MG on the two shafts. Since the MG works as a torque converter with a gear ratio of $G = 2.6$ the two transducers have different nominal torque which have been chosen according to the maximum torque expected during the overload test on the most stressed rotor. In particular, the one mounted on the high speed rotor shaft has a nominal torque of $5Nm$ while the one mounted on the low speed rotor shaft of $10Nm$. The torque transducers are the T21WN produced by HBM. They are represented in figure 3.5 while their principal parameters are reported in table 3.4. The output signal referred to the torque value can be a frequency or a voltage. The output frequency solution was chosen to have a reading less affected by noise.

Figure 3.5: Torque transducer HBM T21WM [14].

Parameter	Value	Unit
Power supply	$10 \div 28.8$	V_{DC}
Accuracy class	0.2	
Nominal torque	[5 10]	Nm
Nominal speed	19000	rpm
Frequency output	$5 \div 15$	kHz
Voltage output	$-10 \div 10$	V
Frequency resolution	0.19	Hz
Voltage resolution	0.38	mV
Voltage source	24	V
Deviation from linearity	$< \pm 0.1$	%
Output frequency for $T = 0$	10	kHz

Table 3.4: Torque transducer HBM T21WM parameters [14].

As it can be seen from the table, the nominal speed is bigger than the one of the motors, so the relative uncertainty of the speed measurement will be very high and special encoders will be necessary to carry out a better measurement.

Encoders

Two incremental magnetic encoders (fig.3.6) produced by RLS with digital output signals have been used to perform the speed measurement. A feeler gauge was used during assembly to check the right distance between the ring and the sensor of $0.1 \div 1.0mm$.

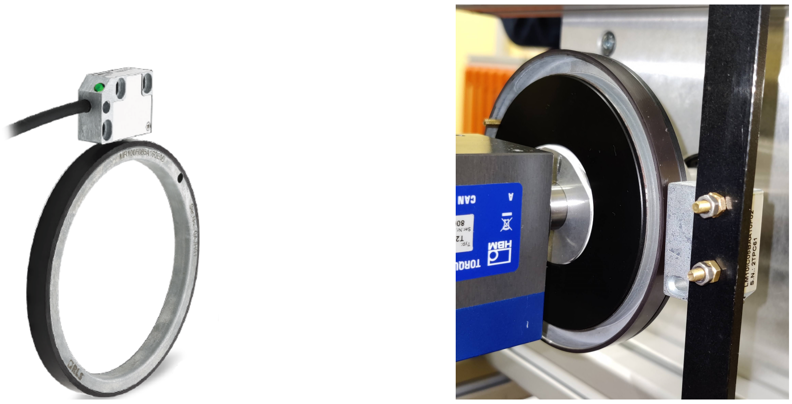

(a) (b)

Figure 3.6: Encoder RLS LM10IC05 [15]. (a) is the figure from the datasheet; (b) is the figure of the encoder mounted on the test bench.

Parameter	Value	Unit
Power supply	$4.7 \div 7$	V_{DC}
Response time	< 10	μs
Signal level High U_H	≥ 2.5	V
Signal level Low U_L	≤ 0.5	V
Switching time (10 to 90%)	< 30	ns
Max cable length	100	m
Output signals (fig.4.5)	3 square-wave signals A,B,Z and their inverted signals A-,B-,Z-	
Reference signals	1 or more square-wave pulse Z and its inverted pulse Z-	

Table 3.5: Encoder RLS LM10IC05 parameters [15].

Cinematic chain

As it can be seen from the figure below, all the components are connected together by means of joints and assembled on the test bench.
On the left of the MG there is the high speed rotor, so the torque transducer with $T_n = 5Nm$, while on the right the low speed rotor with the torque transducer with $T_n = 10Nm$.

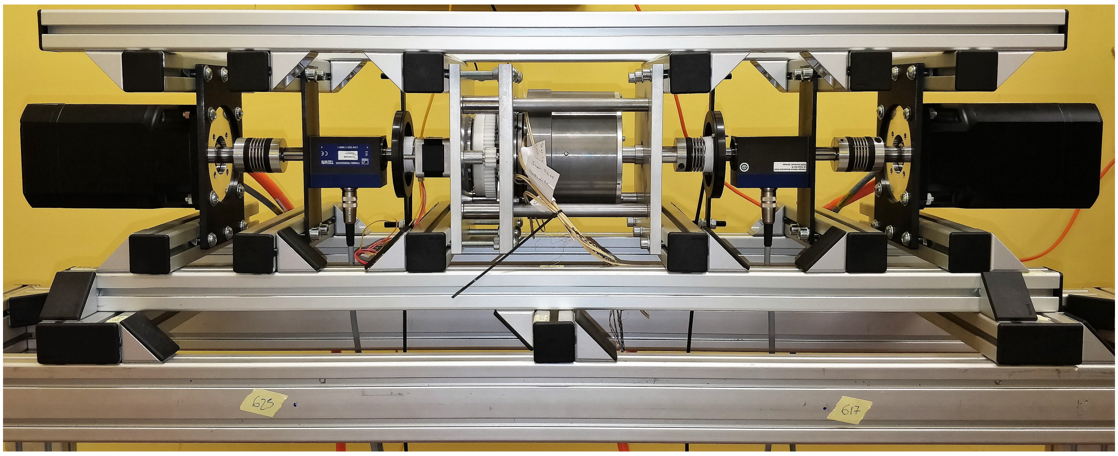

Figure 3.7: Cinematic chain

3.2 Electrical panel

The test bench requires an electrical panel with all the components necessary to supply the electric motors and the measurements tools.

3.2.1 Project

To carry out the project of the electrical panel it is important to know the characteristics of the loads and in particular it is necessary to know their power supply voltage and the power consumption.
In addition to the torque transducers and the encoders described in the previous section, it is necessary to take into account the presence of an electric drive(ED)(rectifier KEN-050N + inverter KWD-5) to supply the motors and the Compact Rio, a component produced by National Instrument, to control it(these components will be well described later). Finally, the power supply of a stepper is planned for future applications.
The table reported the main characteristics of the loads necessary for the project. These data were taken from the datasheets.

Component	Power supply	Power consumption
Torque transducer	24 V_{DC}	12 W
Encoder	5 V_{DC}	0.175 W
Compact Rio	24 V_{DC}	100 W
Stepper	24 V_{DC}	48 W
Heatsink (ED)	24 V_{DC}	5 W
KEN-050N board auxiliaries(ED)	24 V_{DC}	5 W
KWD-5 board auxiliaries(ED)	24 V_{DC}	24 W
KEN-050N board(ED)	400 $Vrms$	5 kW
KWD-5 board(ED)	540 V_{DC}	5 kW

Table 3.6: Main power characteristics of the electric load.

As it can be seen from the table, some converters are necessary to have the 24 V_{DC} and the 5 V_{DC} power supply. It was decided to use 3 converters for the 24 V_{DC} and divide the loads over 3 lines to ensure greater reliability.
Summarizing, there are five different voltage levels:

- 400 V for supply the rectifier;
- 540 V_{DC} for supply the inverter;

- 230 V for supply the converters 230V-24V_{DC} or 230V-5V_{DC};
- 24 V_{DC} for stepper motor, torque transducers, Compact Rio, the auxiliaries of inverter and its heatsink;
- 5 V_{DC} for Encoders.

Finally, a general automatic circuit breaker and fuses on the departures of the various lines have been provided to protect the circuit from any overcurrents.

The following figures are shown larger in the appendices A.

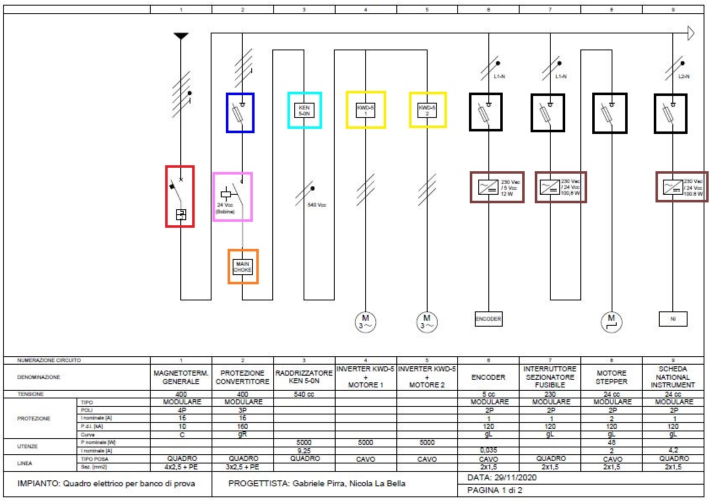

Figure 3.8: Unifilar scheme 1/2.

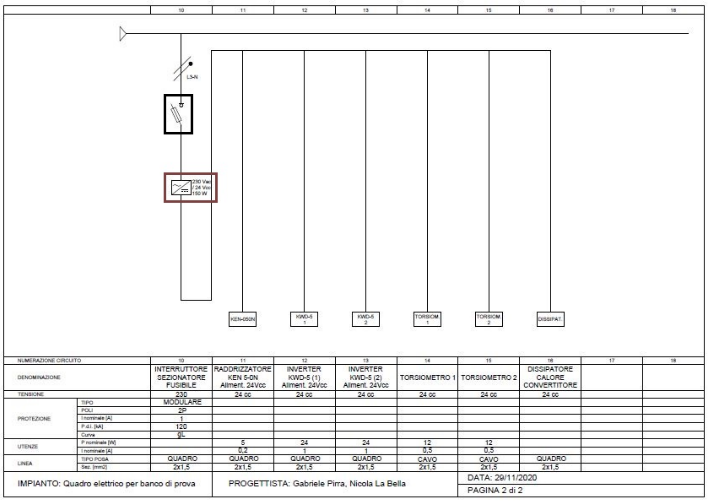

Figure 3.9: Unifilar scheme 2/2.

3.2.2 Components

Terminal block

Sixty pieces of terminal block for din bars have been positioned in the upper part of the electrical panel. Here comes the power from the electric grid and is distributed to all the components. Furthermore, ground terminals are used to connect the components and the electrical panel to the ground network of the Politecnico. This terminal block allows the connection of cables with section up to 4 mm^2 and a maximum current of 32 A.

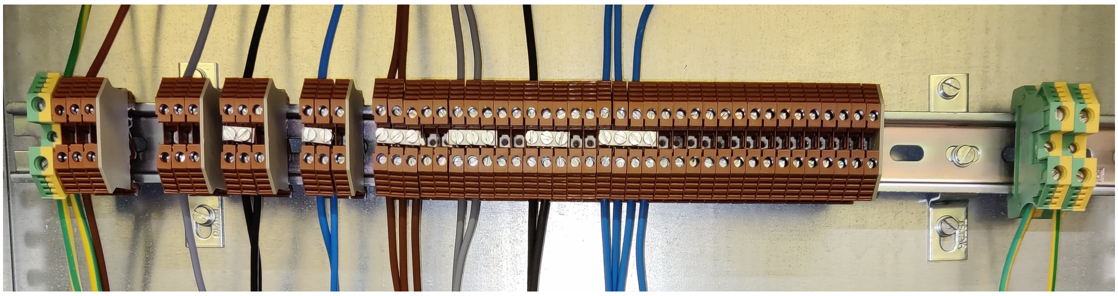

Figure 3.10: Terminal block.

Automatic circuit breaker

A 4 poles automatic circuit breaker was used to protect the entire system from overcurrents. The sizing and choice of the component was made knowing the nominal voltage and nominal current absorbed by the line.

Figure 3.11: Automatic circuit breaker produced by Lovato Electric.

Parameter	Value
Producer	Lovato
Series	P1MB
Poles number	4
Nominal current	16 A
Tripping characteristic	C curve
Nominal voltage	400 V
Breaking capacity	10 kA

Table 3.7: Parameters of automatic circuit breaker produced by Lovato Electric.

Fuse disconnector

Six fuse diconnectors are used to protect the electrical circuit. As shown in the unifilar schemes a 3 poles fuse disconnector protects the three-phase line that powers the motors while five 2 poles fuse disconnectors protect the single-phase lines that power the other loads.
This type of fuse disconnector allows to connect and disconnect the circuit under load condition. In addition, they are compatible with installation on din bars. The tables below show the main parameters of these components.

Figure 3.12: 3P fuse disconnector.

Parameter	Value
Producer	ABB
Poles number	3
Maximum current	32 A
Fuse dimensions	10x38 mm
Fuse current	16 A

Table 3.8: Parameter of the 3P fuse disconnector.

Figure 3.13: 2P fuse disconnector.

Parameter	Value
Producer	ABB
Poles number	2
Maximum current	32 A
Fuse dimensions	10x38 mm
Fuse current	1 or 2 A (Specified in the unifilar scheme)

Table 3.9: Parameter of the 2P fuse disconnector.

Low voltage power supplies

Four converters provide the low voltage power supply for the component listed in table 3.6. In particular one converter provide the 5 V_{DC} power supply while the 24 V_{DC} power supply was provided by one converter with a nominal power of 150 W and two converters with a nominal power of 100.8 W. Images and tables with the main parameters of these converters are shown below.

Figure 3.14: Power supply, 150 W, 24 V_{DC}.

Parameter	Value
Producer	Mean Well
Series	HDR-150
Nominal power	150 W
Nominal input voltage	230 V
Nominal output voltage	24 V_{DC}
Nominal output current	6.25 A
Efficiency	0.905

Table 3.10: Parameter of power supply, 150 W, 24 V_{DC}.

Figure 3.15: Power supply, 100.8 W, 24 V_{DC}.

Parameter	Value
Producer	Mean Well
Series	HDR
Nominal power	100.8 W
Nominal input voltage	230 V
Nominal output voltage	24 V_{DC}
Nominal output current	4.2 A

Table 3.11: Parameter of power supply, 100.8 W, 24 V_{DC}.

Figure 3.16: Power supply, 12 W, 5 V_{DC}.

Parameter	Value
Producer	Mean Well
Series	HDR
Nominal power	12 W
Nominal input voltage	230 V
Nominal output voltage	5 V_{DC}
Nominal output current	2.4 A

Table 3.12: Parameter of power supply, 100.8 W, 5 V_{DC}.

CompactRIO

The CompactRIO is a product made by National Instrument. The CompactRIO is programmed with the software LabVIEW and it exploits the real time communication with the electric drive for the motor control. The communication between the PC and the electric drive takes place through ethernet connection with etherCAT protocol.

Figure 3.17: Controller cRIO.

Input and output signals are managed through the acquisition module NI-9411 for the measures and NI-9421 for emergency.

(a) **(b)**

Figure 3.18: Modules for Controller cRIO: (a) NI-9411, (b) NI-9421.

CompactRIO required 24 Vdc power supply. As is shown in the figure 3.19, the 9411 acquisitions module are connected with specific terminal block on the left that allows to connect the terminals of Encoders and Torque transducers with them. The encoder have 6 cables to be connected: A, B, Z signals and their signals denied. Between the signal and the corresponding denied, it has been connect a resistance of R=250 ohm as the datasheet indicate. The Torque transducers have only two cables to be connected. The card 9421 on the right is an Analog Input card, which is connected with the emergency button in order to warn LabView if a problem occurs. There are also two Ethernet cable in communications with the Pc and the Inverter.

Figure 3.19: CompactRIO.

Electric drive

The electric drive is produced by AMK. The motors are supplied with an alternate three phase voltage of 0-350 V by the drive, which have a nominal power of 5 kVA. As it can be seen from the Figure 3.20 the electric drive has many connections to be done. The electric drive is composed by two modules which are mounted on the heatsink behind. The module on the left is the KEN 5-0N rectifier controller card, while the module on the right is the KWD 5 which contain the two R25 inverter cards. The main connections are:

- Power supply to the motors (2 orange cables - fig.3.20d) connect with the KWD 5. Each cable is composed by the three phases wires, the protection wire and two wires which are connected to the thermal protection (White and Brown - fig.3.20d).
- Sensor of the motor cable (2 grey cables - fig.3.20d) connect whit the R25 cards. It transmit information from the internal encoder of the motor to the inverter.
- Ethercat connections by Ethernet cable between R25 and CompactRIO.
- Three phase power supply connect at the KEN 5-0N from the main choke.
- DC bus at 540 Vdc connections between the two sections of the inverter (Red and Light blue cables - fig.3.20d).

- Other connections with the twisted pair cable for 24 Vdc power supply and the emergency connection with the stop button.

- 24 Vdc to supply the heatsink.

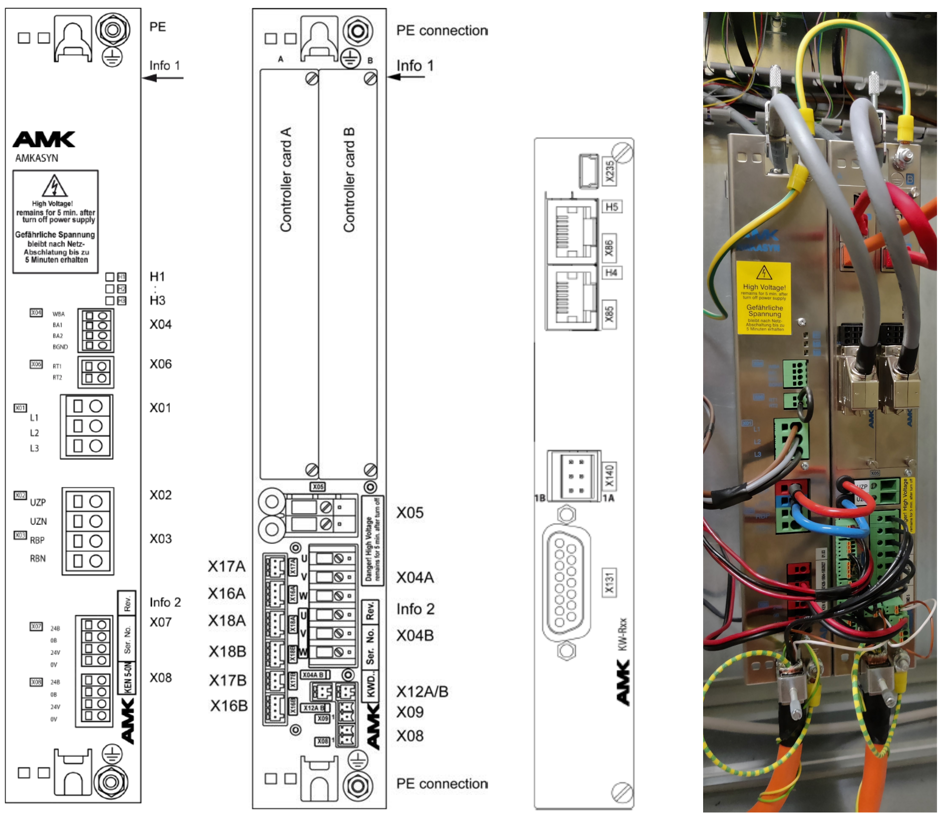

(a) (b) (c) (d)

Figure 3.20: Modules for Controller cRIO [16]: (a) KEN 5-0N, (b) KWD5, (c) r25 controller card, (d) Electric drive. (a-b-c) are shown larger in the Appendix A.5.

Figure 3.21 shows the power diagram of the ED connection. The contactor is used to turn the ED on and off. In particular, the coil of the contactor is energized by acting through a switch located on the control panel. The main choke is an inductance which has the function of filtering the current. The additional brake resistor shown in figure is not used because the internal one is sufficient.

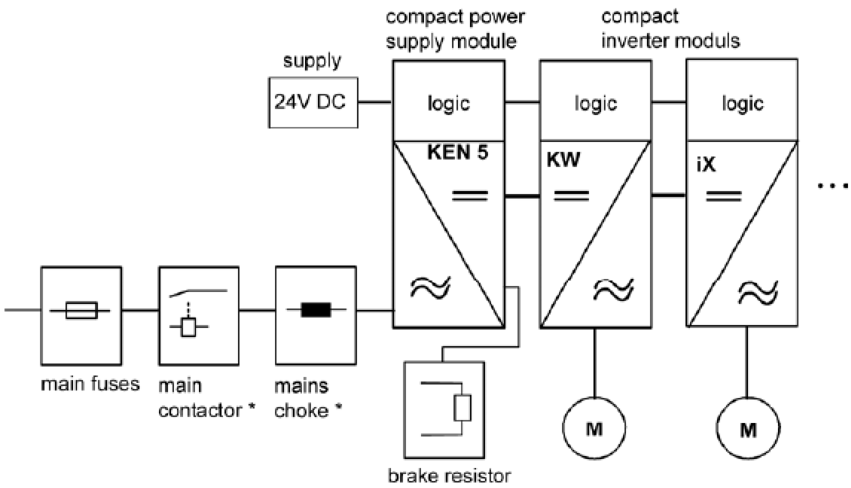

Figure 3.21: Connection diagram of the electric drive [16].

Main choke

This is a three-phase main choke with a nominal current of 12 A. U1, V1 and W1 indicate the input power supply terminals while U2, V2 and W2 the output one. The main choke is inserted before the ED in order to filter the current that will go into the electric grid from the harmonics introduced by the latter, it also guarantees the decoupling between the interacting systems in order to avoid electromagnetic compatibility problems..

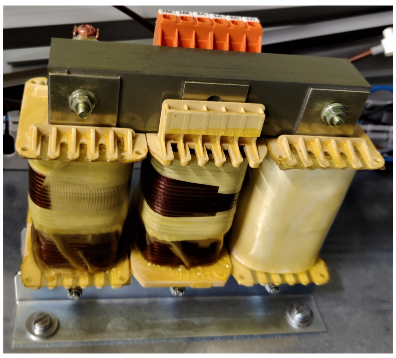

Figure 3.22: Main choke ALN 12.

Contactor

This device is an element capable of stopping or establishing the electric current inside a circuit, opening or closing the contacts between the system and the power

supply. This is very similar to how the switch works.
The change of state of the contacts occurs through the excitation of a coil powered through terminals A1 and A2.

Figure 3.23: Contactor.

Parameter	Value
Producer	ABB
Series	AF09
Poles number	4
Nominal current	25 A
Nominal power	4 kW
Nominal voltage	690 V
Coil voltage	24 $V_{AC/DC}$
Contacts	4 NO

Table 3.13: Parameter of the contactor.

Control panel

As it can be seen from figure 3.24 the control panel is composed by:

- A light to highlight the presence of voltage inside the electric panel.
- A selector to switch on/off the electric drive, which is connect with the contactor.
- Stop emergency button, connected with the inverter and the Analog Input (AI) card on the CompactRIO.
- The ethernet port for connect the PC to the CompactRIO.

Figure 3.24: Control Panel.

3.2.3 Wiring

The composition of the electrical panel start by mounting the cable ducts and din bars with screws on the main panel (fig.3.25a). Then all the components will be placed on the din bars (fig.3.25b) and the main panel will be placed inside the electrical panel.

(a) **(b)**

Figure 3.25: Composition of the electrical panel.

Refering to the figure 3.26 (larger in the appendix A.3) which represent the complete electrical panel, a brief summary of the connections is shown here.
A pentapolar socket connected to the electrical grid provides power to the electrical panel through the terminal blocks (squared in green).
The first component is the automatic circuit breaker (squared in red), which has the function of protect the entire electric line from overload and short circuits. After the automatic circuit breaker the electric line is divided in five sections. In according with the unifilar scheme reported above in Figure 3.8 and Figure 3.9, the first section is the three phase power supply of the motors. Proceeding in order the first component is the fuse disconnector (squared in blue), which has the function of protect the line from overcurrents. After that there is a contactor (squared in pink), with a coil supplied with the 24 Vdc, that allow to turn on the electric drive when the switch on the control panel is turned on. Before the electric drive there is the main choke (squared in orange) as indicated on the datasheet which has the function of filtering the current. The electric drive is composed by three

controller cards, the KEN 5-0N rectifier (squared in light blue) which convert the voltage to 540 Vdc and the KWD-5 inverter module (squared in yellow) with two r25 cards that feed the motors. An emergency button stopped the motors when a problem occur, the inverter goes in the emergency state and the IGBTs (Insulated Gate Bipolar Transistor) are opened, so the power supply is disconnected. The nominal current is 16A because, even if the motors have a nominal power of 5 kW each, one of that is working in the break mode, so the power is exchange from one motor to the other one without absorb huge current from the line. The other four sections are the low voltages lines. The conversion from 230 V to 24 Vdc and 5 Vdc was made with four converters (squared in brown). The loads have been diveded in order to keep the line balanced. All the sections are protected by fuse disconnectors (squared in black), which have been sized in according with the nominal current absorbed by the respective section. The converters have a short circuit protection inside of them, so only the line that feed the stepper motor has also a fuse disconnector after the converter, this is due to the fact that this is the only one that can risk an overload.

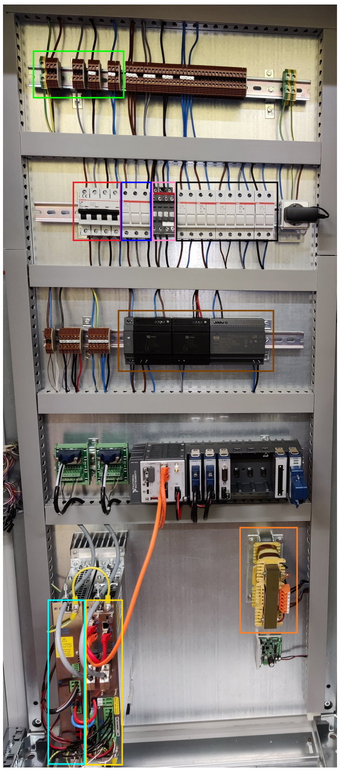

Figure 3.26: Electrical panel.

An overview of the complete test bench is shown in the appendix in figure A.4.

Chapter 4

Software

4.1 Data acquisition method

The data to be acquired to evaluate the operation of the magnetic gear are:

- the radial and circumferential flux and magnetic induction inside the MG.
- the torque on the two shafts of the MG.
- the speed of the two shafts of the MG.

4.1.1 Flux and magnetic induction

The magnetic flux behavior inside the magnetic gear can be reconstructed from the measurement of the induced voltage in the radial and tangential coils inserted on the carrier around the ferromagnetic pole pieces described in chapter 2.2 knowing that the link between the two quantities is described by the Faraday-Neumann-Lenz law:

$$emf = N \cdot \frac{d\Phi}{dt} \tag{4.1}$$

The induced voltage was measured by the digital oscilloscope shown in figure 4.1, then the data were saved and exported to Matlab to be processed and obtain the waveforms of fluxes and magnetic induction that will be reported in chapter 5.2. The magnetic induction is computed knowing the cross section areas of the two coils.

$$B = \frac{\Phi}{S} \tag{4.2}$$

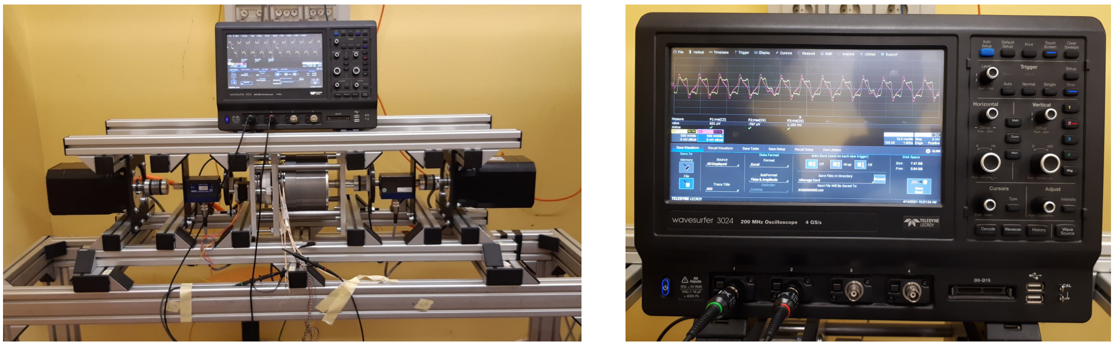

(a) (b)

Figure 4.1: Oscilloscope.

4.1.2 Torque

As described in section 3.1.2, the torque transducer outputs a frequency signal between 5 and 15 kHz. In particular, an output signal with a frequency of 5 kHz will correspond to the negative nominal torque of the transducer while a 15 kHz signal will correspond to a positive torque value equal to the nominal torque. For a zero torque value the output will be a 10 kHz signal with an uncertainty of 50 Hz. The sensitivity of the torque transducer is 0,19 Hz. The figure 4.2 below shows an example of an output signal when the torque value changes. As can be seen, as the torque value decreases, the frequency of the output signal will also decrease.

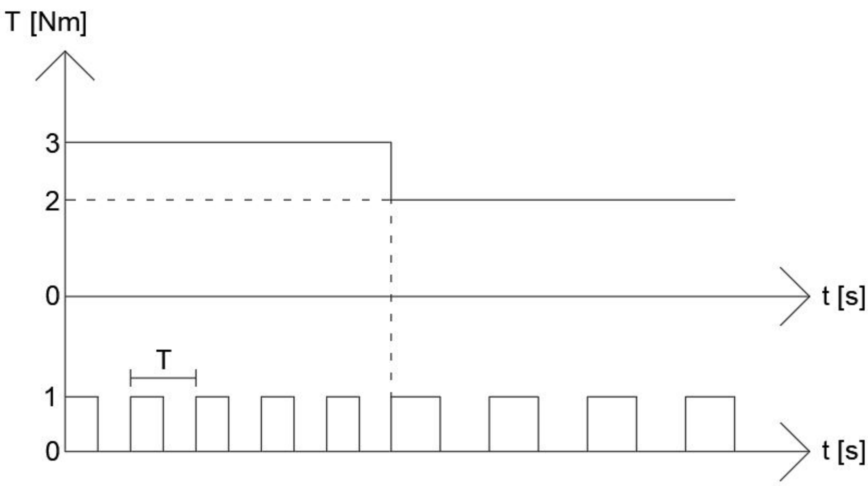

Figure 4.2: Example of an output frequency signal when the torque value changes.

Since the signal can be subject to disturbances due to the length of the cable with which it is transmitted, the square wave reference signal and its negated will be output from the torque transducer. These two signals will be acquired by the NI 9411 card and as can be seen from figure 4.3 the original signal will be reconstructed by canceling the common mode error by applying the difference of the two input signals.

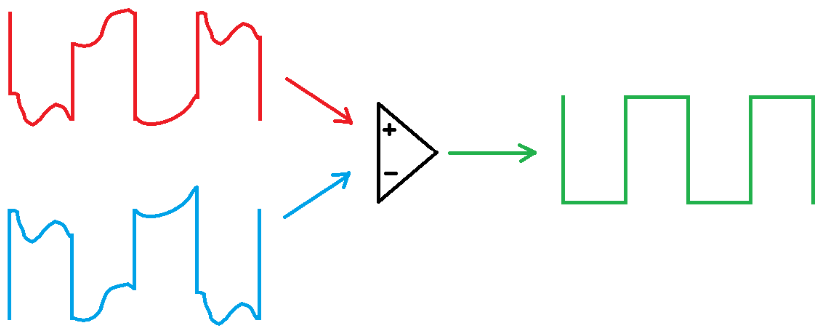

Figure 4.3: Example on how common mode disturb comes cut off by comparing 2 opposite signals.

At this point it is necessary to understand how to acquire the frequency signal with the NI 9411 card. With the CompactRIO used in this test bench, it is possible to use the DAQmx driver with its blocks to make acquisitions using the LabVIEW programming software. The main element is certainly the counter which has the function of defining the frequency value of the input signal. The logic diagram shown in the figure below shows the main elements of the conversion. As it can be seen, the frequency value of the output signal from the torque transducer is read with a certain sampling frequency f_s and the value is saved in the counter register. The data is subsequently passed to the FIFO(First In First Out) memory and then to the buffer of the RAM memory via BUS channel. Every N data present in the buffer they are extracted and represented on a graph. The graph will then update with a period of $T = N/f_s$. It is very important to choose a correct value of the sampling frequency to acquire the signal. In particular, the maximum period of the square wave input signal is equal to $T = 1/5000 = 0.2ms$, corresponding to the frequency of 5 kHz. It will be necessary to wait for a value greater than the latter to carry out the sampling, therefore a value $f_s = 1$ kHz was chosen.

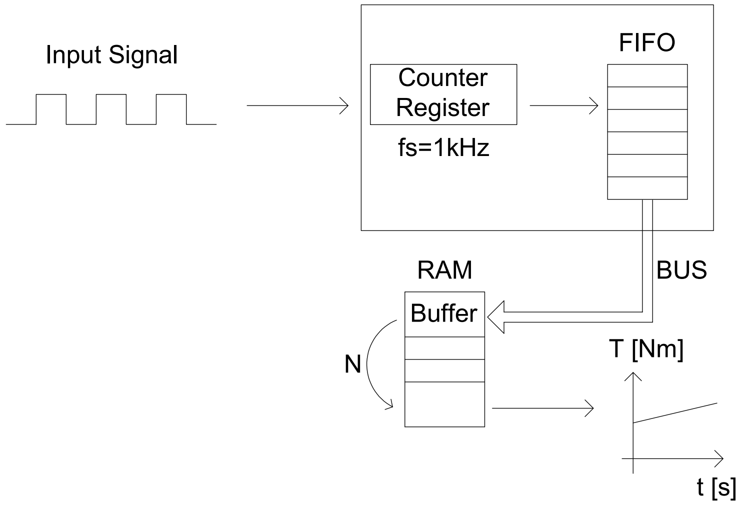

Figure 4.4: Logic diagram of torque acquisition.

4.1.3 Speed

The magnetic encoder described in section 3.1.2 outputs the signals A, B, Z and its negated. As for the torque transducer, the input signals will be acquired by the NI 9411 card and will first be reconstructed having both the reference signal and its negated one and subsequently processed to obtain the speed measurement. As can be seen from the figure 4.5 below, the signals A and B are square waves out of phase by a quarter of a period. According to the phase difference between the two signals, it is possible to understand the direction of rotation of the encoder(fig.4.6). The signal Z is instead a single pulse for each complete revolution of the incremental encoder and provides information on the reference zero position.

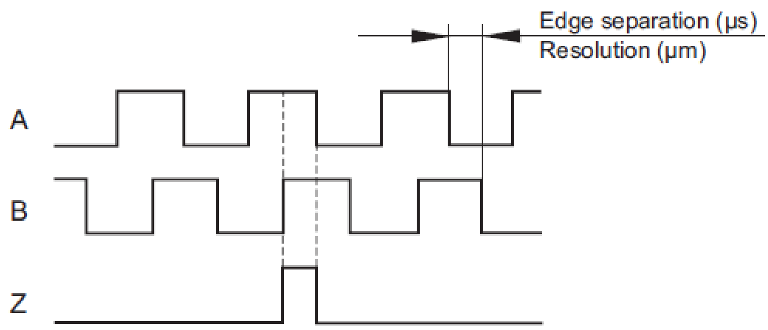

Figure 4.5: Encoder timing diagram (complementary signals not shown)[15].

In order to obtain the value of the angle of the position in which the encoder is located, it is important to know its resolution. In particular, the number of counts per revolution(cpr) is calculated using the following equation indicated in the datasheet [15]:

$$Resolution(cpr) = PoleNumber \cdot interpolation = 160 \cdot 32 = 5120cpr \tag{4.3}$$

while the number of pulses per revolution (ppr) is obtained knowing that the counting resolution is increased by 4 times having both the A and B signals, indeed, a pulse is generated at each rising or falling transient of the two signals(CLK in fig.4.6) and these pulses feed a position counter PCNT that increases or decreases his count depending on the direction of rotation:

$$Resolution(ppr) = \frac{cpr}{4} = \frac{5120}{4} = 1280ppr \tag{4.4}$$

Finally, to compute the value of the angle of the position in which the encoder is located, it will be sufficient to multiply the multiplication factor that describes the angle variation for each pulse by the count:

$$\theta_{enc} = \frac{2\pi}{ppr} \cdot PCNT = \frac{2\pi}{1280} \cdot PCNT \tag{4.5}$$

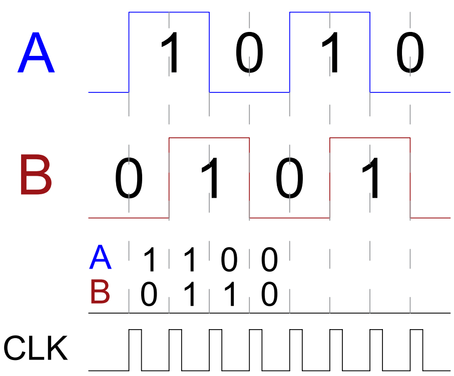

	clockwise	counter clockwise
A	1 1 0 0	0 0 1 1
B	0 1 1 0	0 1 1 0

Figure 4.6: Channels A and B and direction of rotation.

The encoder speed is obtained by discrete-time derivation of the encoder position signals, which can be approximated with the function sin to avoid the effect of discontinuity of 2π at the reference position given by the pulse signal Z:

$$\omega_{enc}(k) = \frac{\theta_{enc}(k) - \theta_{enc}(k-1)}{T_{enc}} \cong sin[\theta_{enc}(k) - \theta_{enc}(k-1)] \cdot f_{enc} \tag{4.6}$$

4.2 LabVIEW working environment

LabVIEW is a system design software designed specifically for developing test, measurement, and control applications with quick access to hardware and results. The LabVIEW programming environment simplifies hardware integration for engineering applications to provide a uniform methodology for acquiring data from NI and third-party hardware. LabVIEW allows you to reduce programming complexity by allowing you to focus on individual tasks. LabVIEW allows you to quickly visualize results thanks to the drag-and-drop creation of user interfaces. The programming language used in LabVIEW differs from traditional languages because its syntax is not written but graphic, and for this reason it is called G-Language (Graphic Language). A program realized with LabVIEW is called VI(Virtual Instrument). The two main parts of the VI are:

- the Block Diagram
- the Front Panel

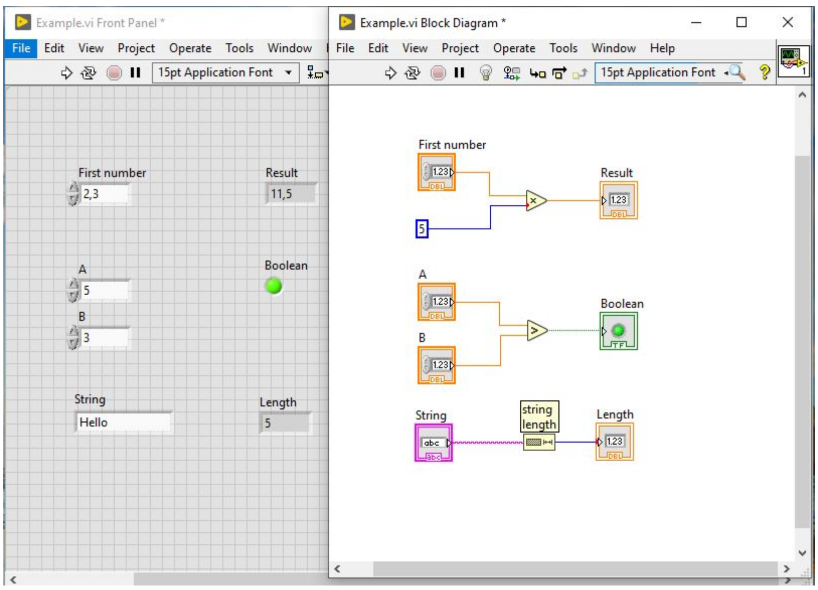

Figure 4.7: Example of a LabVIEW VI.

4.2.1 Block Diagram

The block diagram contains the graphical source code of a LabVIEW program. The concept of the block diagram is to separate the graphic source code from the user interface. As it can be seen from figure, the 'Function' palette contains all the blocks useful for creating the program. The main blocks are terminals, subVIs, functions, constants, structures, and wires that transfer data among other block diagram objects. It is possible to insert objects in the block diagram simply by using drag and drop. The colors of the connecting cables between the various blocks describe the type of data they transfer and are divided into:

- Orange for floating point numeric data.
- Blue for integers.
- Green for boolean data.
- Pink for strings.

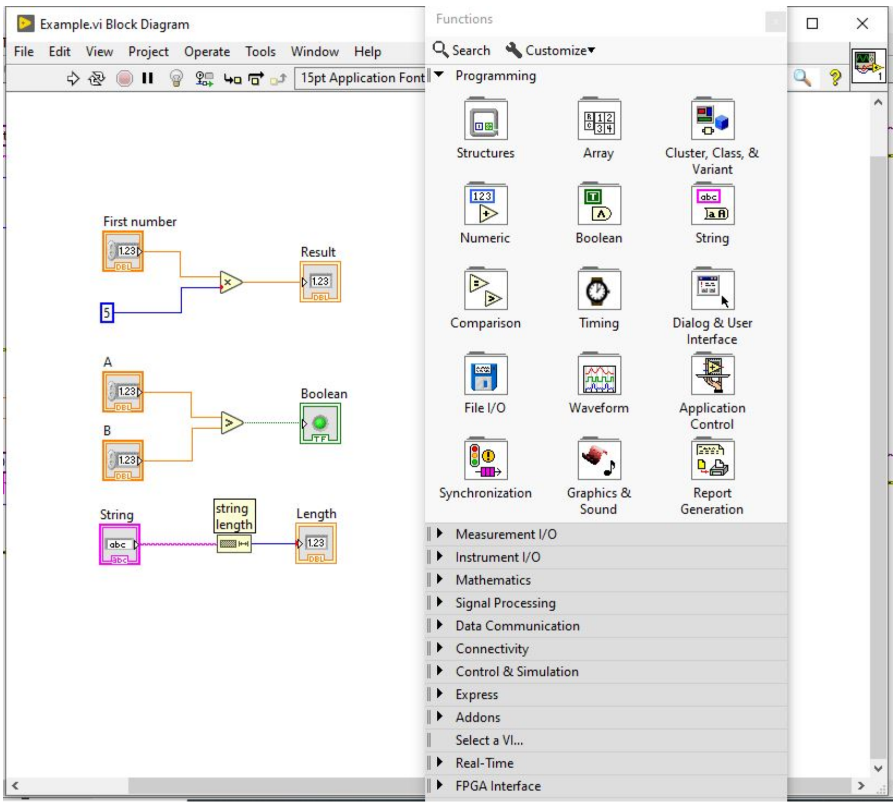

Figure 4.8: Example of a LabVIEW VI block diagram.

4.2.2 Front Panel

The front panel window is the user interface for the VI. The front panel has controls and indicators, which are the interactive input and output terminals, respectively, of the VI. Controls and indicators placed on the front panel are automatically placed on the block diagram. By right clicking anywhere on the front panel the 'Controls' palette opens. It is possible to insert objects in the front panel simply by using drag and drop. Controls such as knobs, buttons, dials, and other input devices are the interactive input terminals, while indicators such as graphics, LEDs, and other displays are the interactive output terminals of the VI. As for the block diagram, these controls can be associated with boolean data, integers, strings or floating point numeric data. At the top of the front panel window, the toolbar contains buttons for running and editing the VI. To run the VI you need to press the 'Run' button. 'Run Continuously' button run the VI until the abort or pause execution buttons are pressed. 'Abort Execution' button stop the VI immediately, but it is suggested to program the VI in another way to stop it.

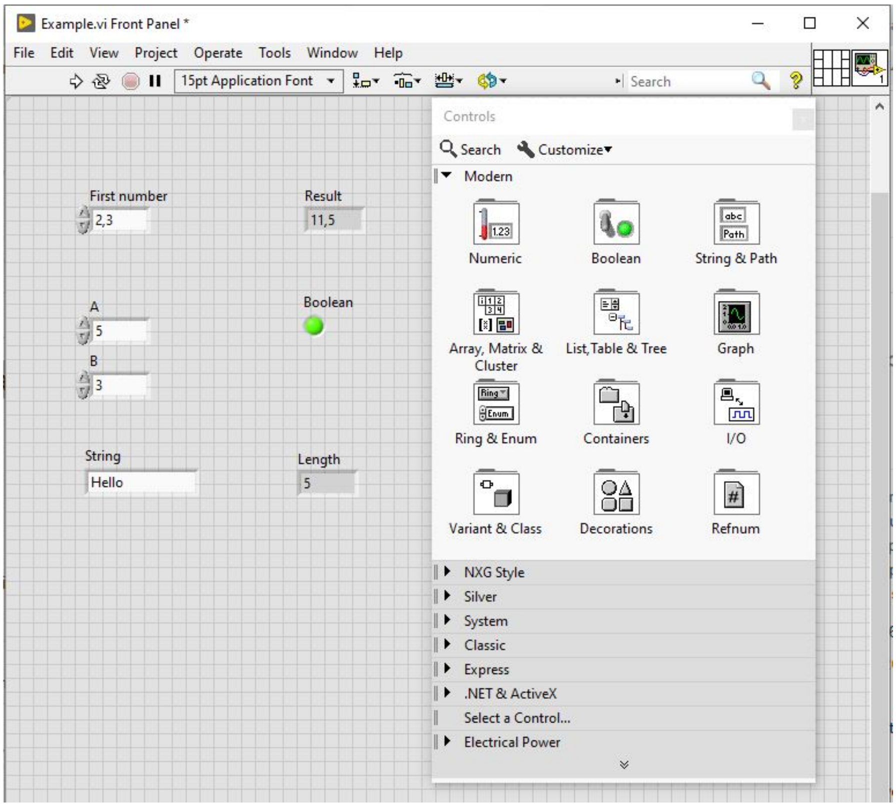

Figure 4.9: Example of a LabVIEW VI front panel.

4.3 LabVIEW test bench program

For the realization of the program used for the acquisition of the signals through the NI 9411 cards mounted on the Compact Rio, the DAQmx driver is of fundamental importance. This driver makes it possible to use hardware components such as NI cards to perform acquisitions and also introduces a series of blocks in the function palette (fig.4.10) of the block diagram that simplify programming the VI.

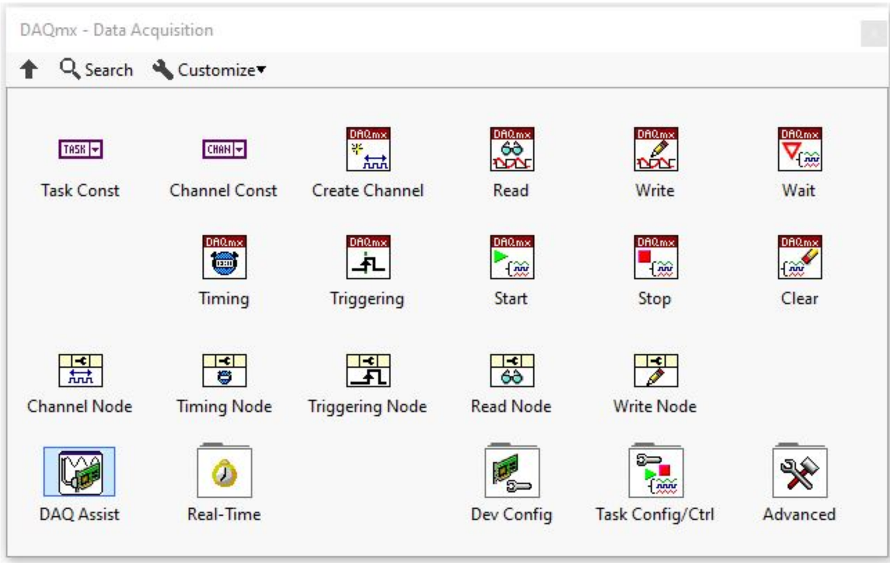

Figure 4.10: NI DAQmx blocks for data acquisition.

The main blocks used are (figures with all the parameters to be chosen can be found in the appendix B.1):

- DAQmx Create Virtual Channel: creates a virtual channel or set of virtual channels and adds them to a task. This is a polymorphic VI so the name and the type of the channel (I/O analog, digital or counter channel) are here declared in addition to other parameters that can be better consulted in the figure B.1. The instance 'CI Freq' creates a channel to measure the frequency of a digital signal while 'AI Voltage' creates a channel to measure an analog voltage.

- DAQmx Timing: Configures the number of samples to acquire or generate and creates a buffer when needed. The instance 'Sample Clock' sets the source of the Sample Clock, the rate of the Sample Clock, and the number of samples to acquire or generate (fig.B.2).

- DAQmx Start Task: Transitions the task to the running state to begin the measurement (fig.B.3).
- DAQmx Read: Reads samples from the task or virtual channels you specify. The instances of this polymorphic VI specify what format of samples to return, whether to read a single sample or multiple samples at once, and whether to read from one or multiple channels. The instance 'Counter 1D DBL 1Chan NSamp' reads one or more floating-point samples from a counter task while 'Analog 1D DBL 1Chan NSamp' reads one or more floating-point samples from a task that contains a single analog input channel (fig.B.4).
- DAQmx Clear Task: clears the task (fig.B.5).

Using the blocks described above, it is possible to create a simple program for acquiring a torque signal following the logic diagram shown in figure 4.4.

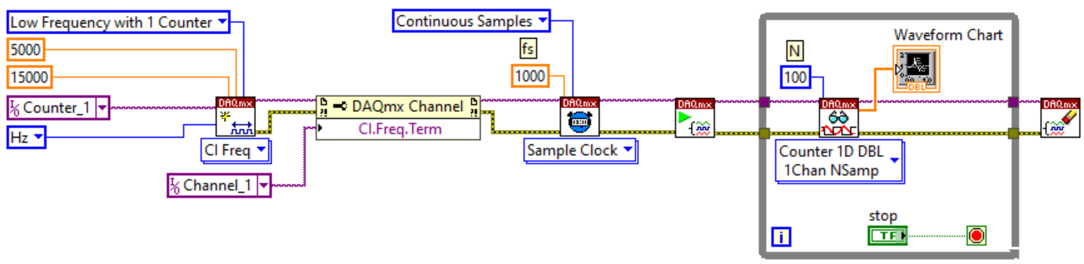

Figure 4.11: Example of VI program for torque signal acquisition.

The figure above represents an example and the starting point for the acquisition of the signals to be measured. The program was then implemented and improved until it reached the final shape that is still used to carry out the measurements on the test bench. In this thesis not all the code of the final program is described, but a look at the front panel is carried out below.
2 programs have been developed for the functioning of the test bench: the first has been programmed to communicate with the electric drive through the CompactRIO and to be able to control the motors, the second instead is the one used to carry out the acquisitions.

4.3.1 Front panel VI for motors controlling

The front panel of the VI for control the motors is divided in four main sections.

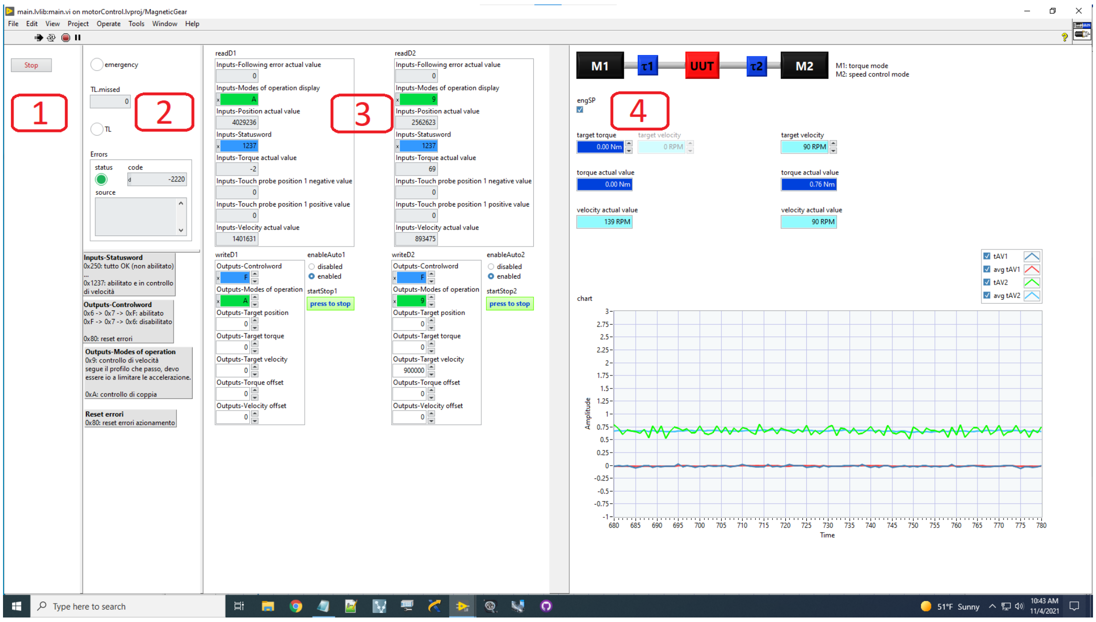

Figure 4.12: Front panel VI for motors controlling.

In the first section there is the Stop button to stop the program at any time. The second section contains the indicators on the operating status of the test bench. If the emergency button on the control panel is pressed, the red 'emergency' LED will light up (fig.4.13a). There are also notes on the codes displayed or to be entered in the respective fields of section 3 (fig.4.13b).

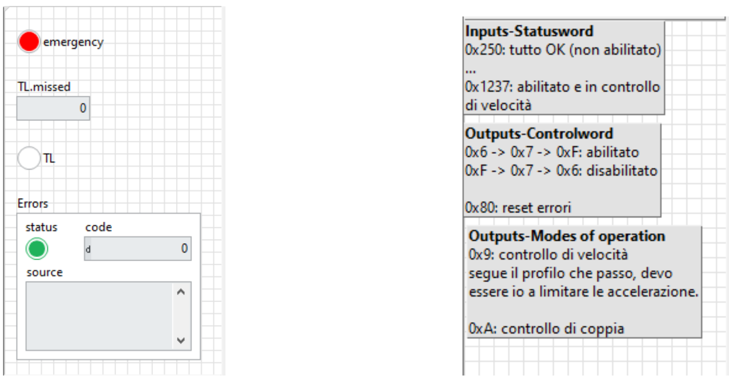

(a) **(b)**

Figure 4.13: Front panel VI for motors controlling (Second section).

In section 3 it can be find the instantaneous and reference torque and speed values set, in addition to other values useful for evaluating the functioning of the test bench. The codes that describe the operating status and operating mode of the test bench are entered or represented in the green and blue boxes, in accordance with the notes in figure 4.13b. Finally there are the controls to enable and start the two motors.

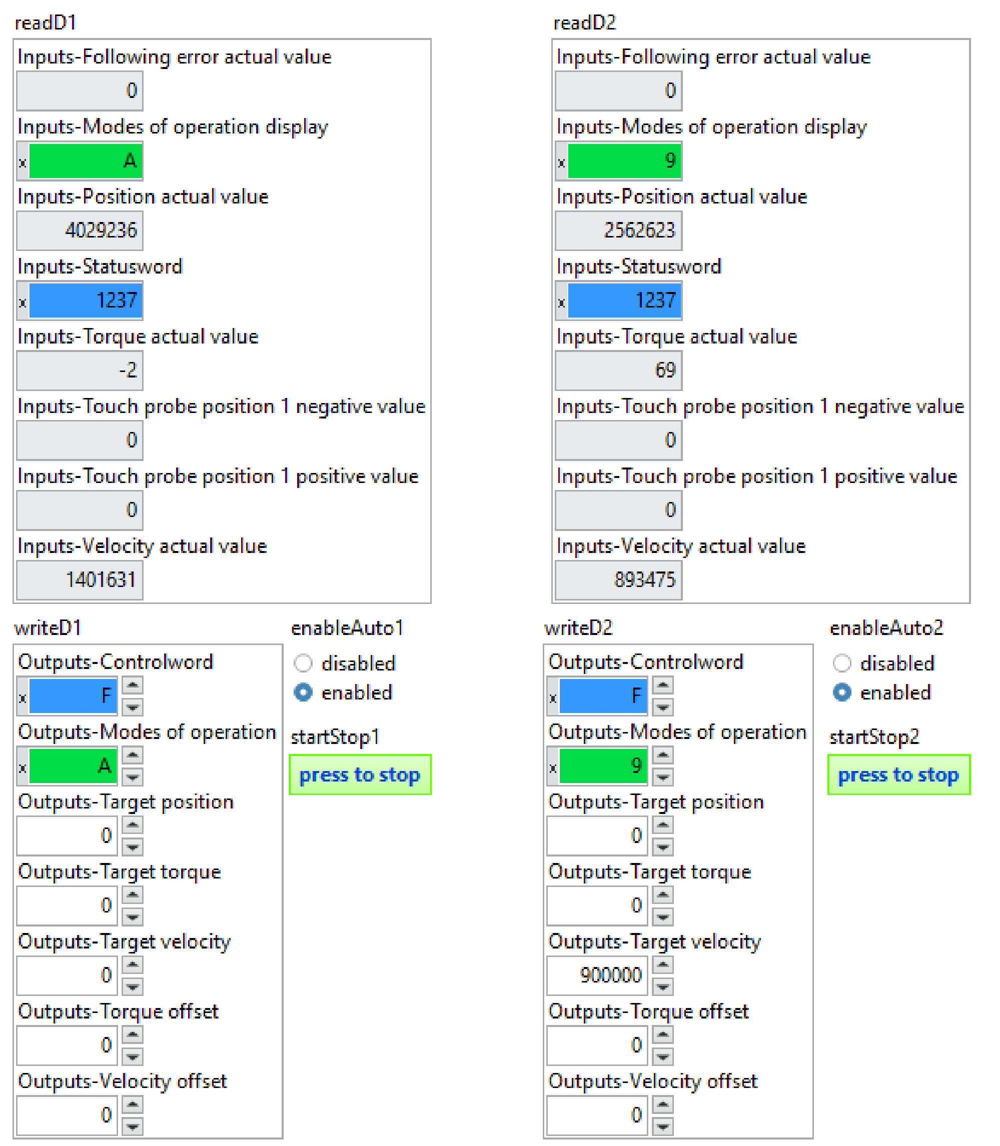

Figure 4.14: Front panel VI for motors controlling (Third section).

Section 4 is the one that allows the real control of the motors. In particular, here it is possible to enter the reference torque and speed values, after having checked the 'engSP' box. In no load tests, where one of the two motors is disconnected, the speed target of the connected motor is set to carry out the measurements. In ordinary operation, on the other hand, the motor M1 will be driven in torque mode while M2 in speed mode, this is to prevent the system from diverging. Finally, a graph represents the instantaneous and average torque values (not those read by torque transducers).

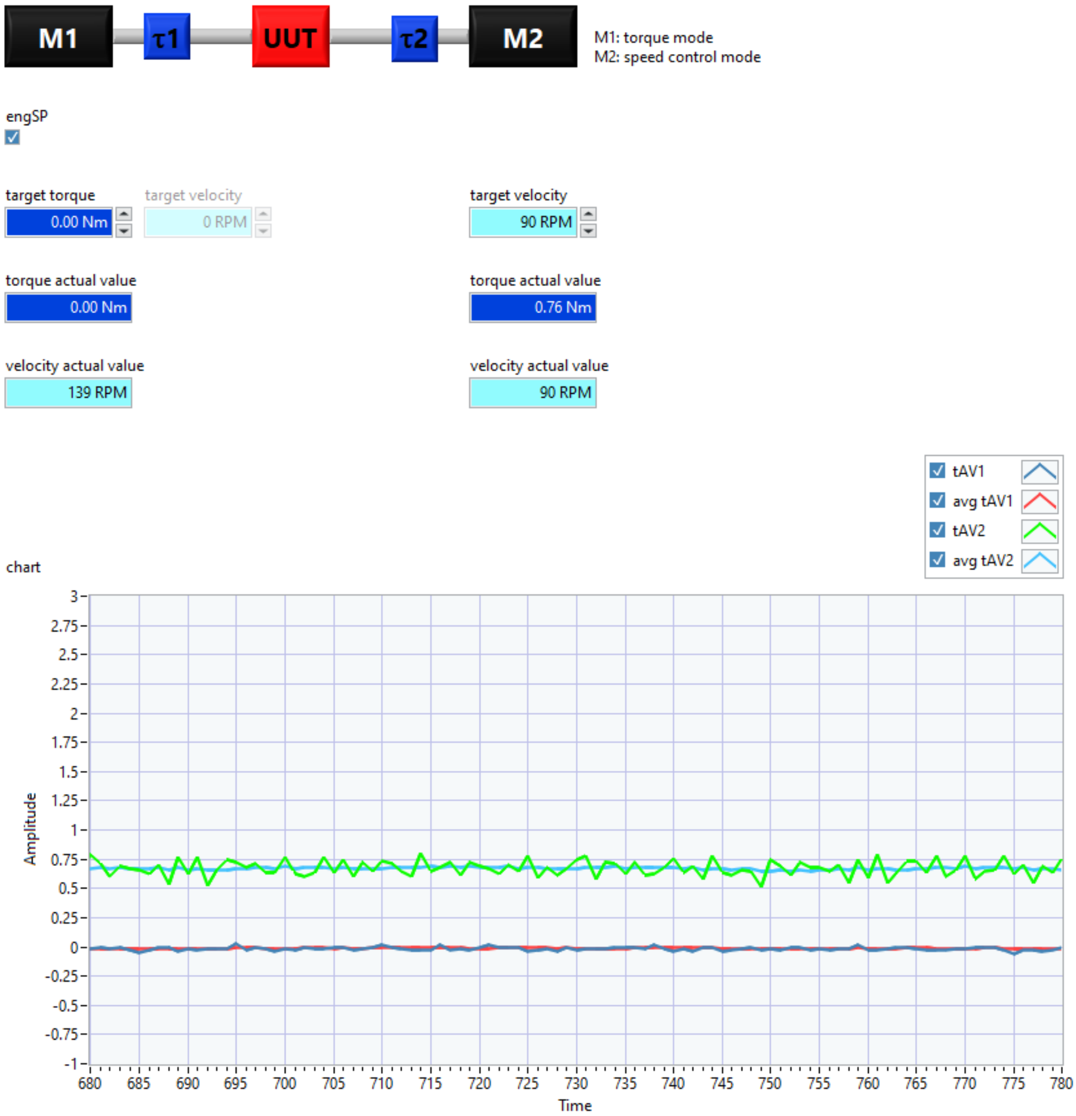

Figure 4.15: Front panel VI for motors controlling (Fourth section).

4.3.2 Front panel VI for acquisitions

The front panel of the VI for acquisitions is divided in two main sections.

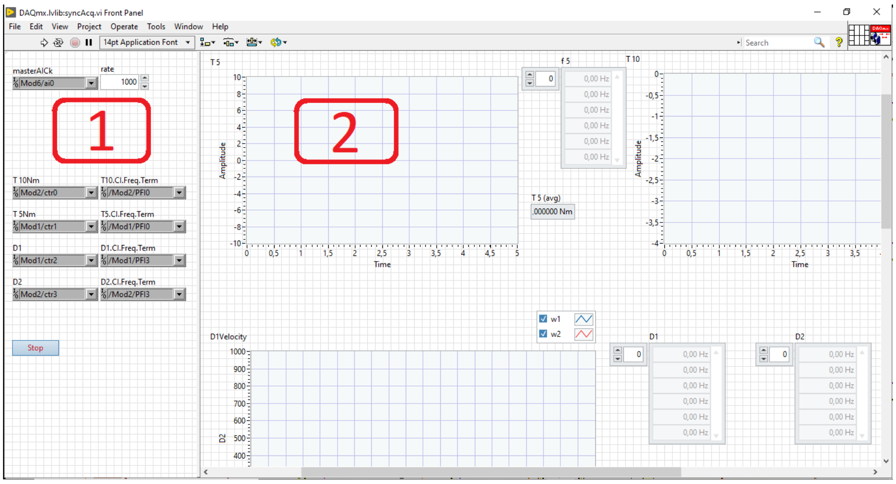

Figure 4.16: Front panel VI for acquisitions.

As it can be seen from the figure below, in the first section the channels used to carry out the acquisitions are set. In particular, starting from the top, it can be observed that a channel of an Analog Input acquisition card has been defined, in fact, to generate the clock to carry out the measurements, the acquisition at 1 kHz was simulated by means of an analog acquisition card for then use the acquisition pulses of the latter as a 1 kHz clock for the other cards described above. Then the used counters and the input channels of the signals coming from encoders and torque transducers are set. Finally, the Stop key to stop the acquisition at any time.

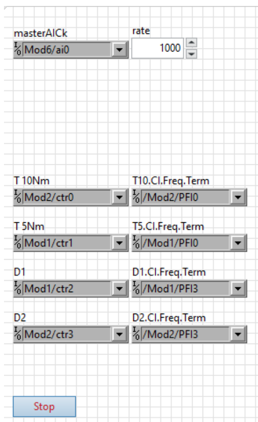

Figure 4.17: Front panel VI for acquisitions (First section).

Two graphs show the waveform of the torques acquired by the two torque transducers. In addition, the average torque value and the acquired instantaneous frequency values are shown. On the left are the values referring to the 5 Nm torque transducer while on the right those referring to the 10 Nm torque transducer.

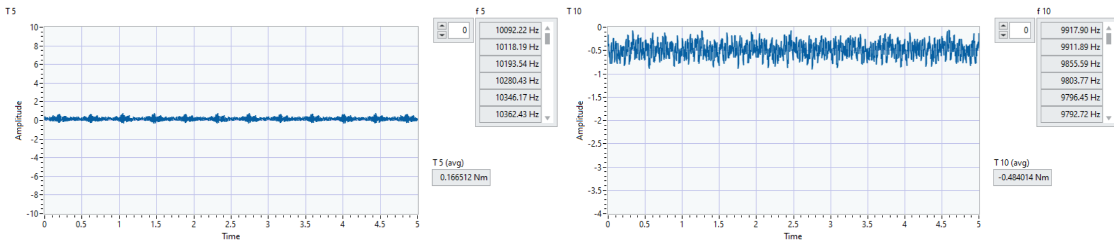

Figure 4.18: Front panel VI for acquisitions (Second section 2.a).

The two speeds acquired by the encoders are represented on a single graph. The average speed values and the instantaneous frequency values are shown here. In addition, a status led warns in case of error.

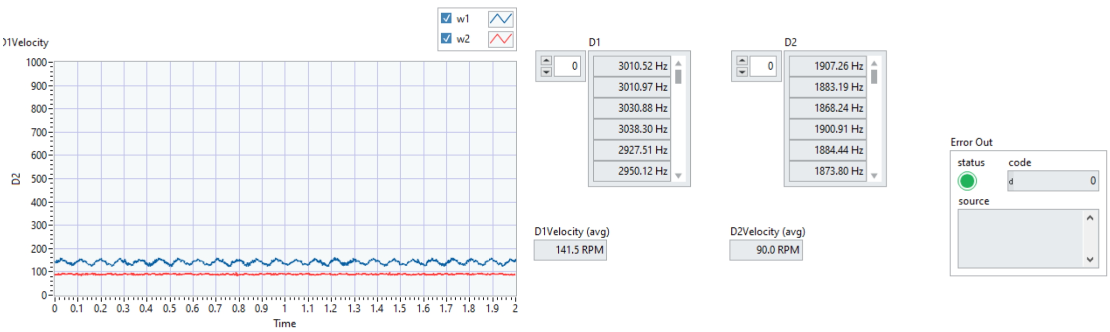

Figure 4.19: Front panel VI for acquisitions (Second section 2.b).

Finally there is an overall graph with all the acquired torques and speeds and an underlying graph representing the Fourier harmonic spectrum of the torques.

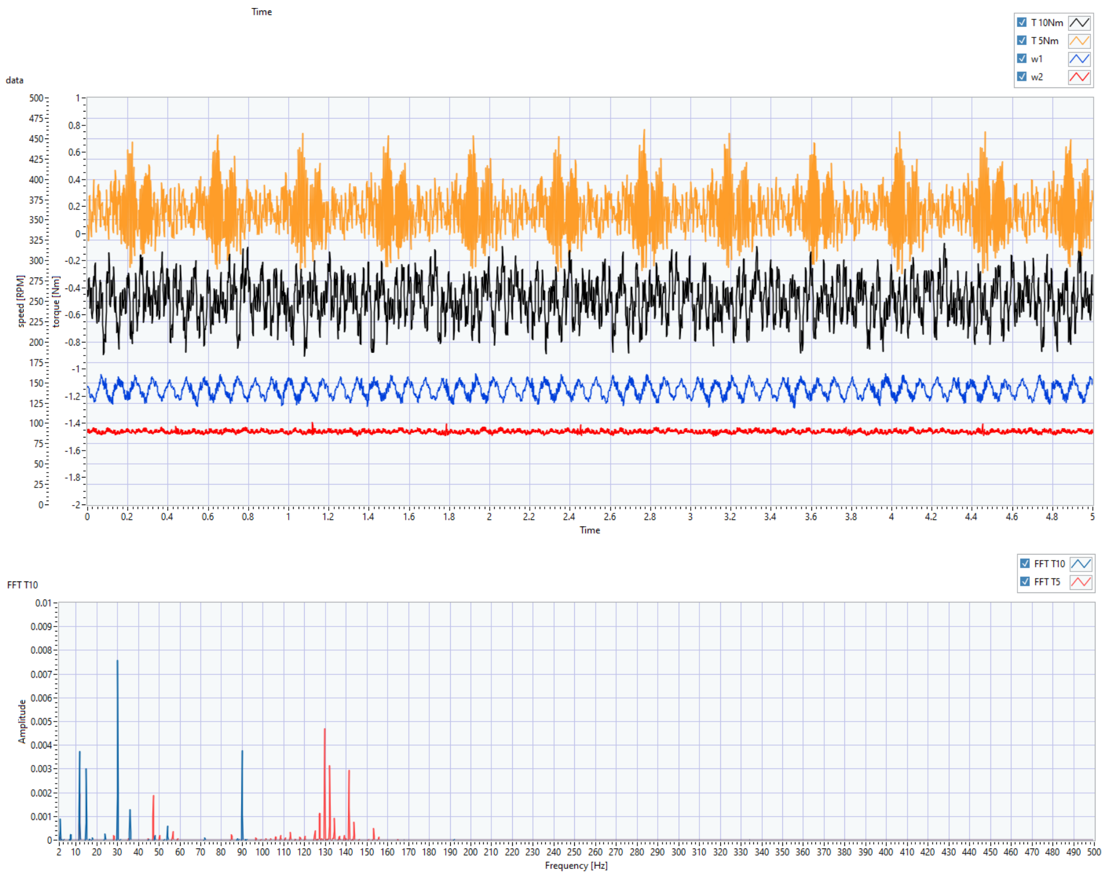

Figure 4.20: Front panel VI for acquisitions (Second section 2.c).

Chapter 5

Experimental and numerical results

5.1 Procedure for experimental tests

The steps to follow to start the test bench and carry out the measurements are reported here:

1. Before connecting the pentapolar socket to the grid, make sure the automatic circuit breaker is on and all fuses inserted.
2. Connect the pentapolar socket to the electrical grid to power the electrical panel. The white light on the control panel should turn on.
3. Connect the PC to the Compact Rio via the ethernet port on the control panel.
4. Turn on the electric drive using the switch on the control panel.
5. Open the VI for motor controlling and run it.
6. Set the mode of operation of the two motors in the section 3 of the front panel and enable the motors (fig.4.14).
7. Set the target value of torque and speed in the section 4 of the front panel (fig.4.15) after checking the 'engSP' box. Remember that the M1 motor must be controlled in torque mode while M2 in speed mode. Only when the no load test is performed is it possible to command M1 in speed mode (in this case M2 is disconnected and the target speed can be set, preventing the system from diverging). Make sure not to exceed the nominal values of the measuring instruments used. The MG has inherent overload protection.

8. Open the VI for acquisitions and run it.
9. The measured torque and speed values will start to be read and displayed.

The steps to follow to stop the test bench are reported here:

1. Press the Stop button on the front panel of the VI for acquisitions and close it.
2. Reset the motor torque and speed targets to zero from the VI front panel for motor control.
3. When the motors have stopped, press the Stop button and close the VI.
4. Switch off the electric drive using the switch on the control panel.
5. Disconnect the pentapolar socket from the grid to cut off the power supply from the electrical panel.

In case of emergency, press the STOP button on the control panel to send the electric drive into protection and stop the test bench.

5.2 Simulation results

Waveforms magnetic properties of magnetic flux and induction have been simulated with static simulations changing the angular position of inner and outer rotors of the magnetic gear, at different distances in radial direction for each component which is part of the magnetic gear.
The simulation has been done with the FEMM software. A complete rotation of the sun is done with a degree step of 0.25°, so on all the figures five periods for each magnetic quantity can be seen, since the number of PMs pole pairs on the inner rotor is five. To be clear, angular positions of the sun in which the various quantities have been evaluated are reported in the vector:

$$\theta_s = [0° : 0.25° : 360°]$$

The angular positions of the ring are linked to those of the sun through the transmission ratio, furthermore the nominal torque constraint is imposed, so the angular positions of the two rotors must change moving on an oblique line of maximum torque that can be seen from graph 2.6. The vector of the positions of the ring is therefore:

$$\theta_r = [\theta_{r,max} : -\tfrac{0.25°}{2.6} : \theta_{r,max} - \tfrac{360°}{2.6}]$$

The minus sign is due to the fact that the two rotors are counter-rotating.

5.2.1 Voltage

As can be seen form the figure below, the electromotive force is not sinusoidal, this is due to the harmonics inside the magnetic flux. As is known, the amplitude of the emf depends on the rotating speed of the rotor, so it must be keep in mind that the figure below, which has the waveforms with a peak of about 1000 mV, is the result of a simulation with a speed of the sun of 600 rpm.

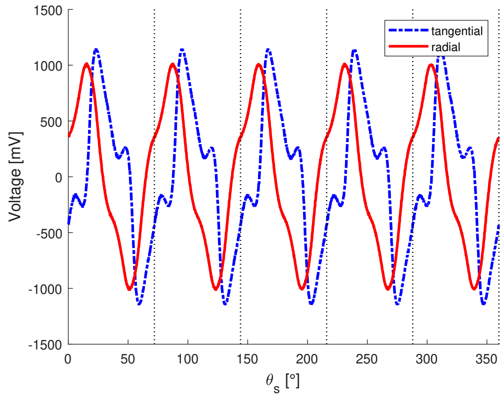

Figure 5.1: Electromotive force simulated at $\omega_{sun} = 600rpm$.

5.2.2 Magnetic flux

The figure below represents the waveforms of radial and tangential magnetic flux inside the ferromagnetic pole.

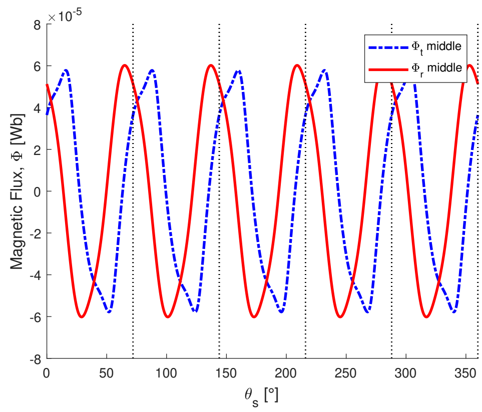

Figure 5.2: Tangential and radial magnetic flux simulated.

5.2.3 Magnetic induction

The figures below show the radial and tangential induction waveforms as a function of the sun angle evaluated in five different points of the ferromagnetic pole. $x_{pole} = 0$ means the innermost point of the pole and therefore the closest to the inner rotor, while $x_{pole} = th_{pole}$ the outermost point and therefore the closest to the outer rotor. As it can be seen in figure 5.3 and 5.4 , the amplitude of the radial magnetic induction is similar for all the points, while that of the tangential magnetic induction decreases moving away from the inner rotor.

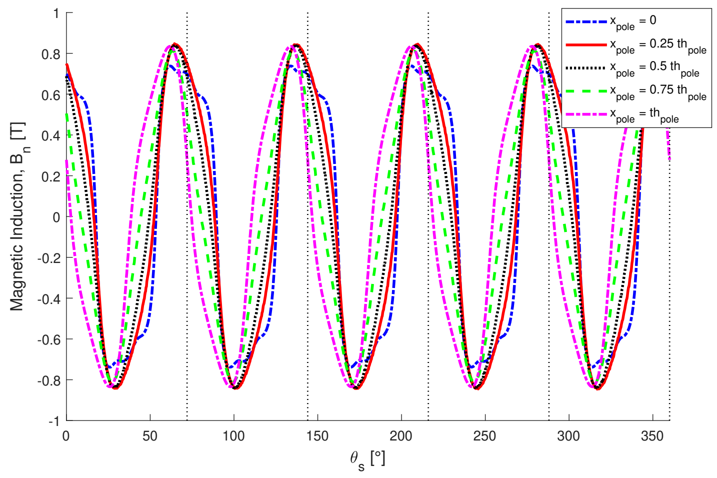

Figure 5.3: Radial magnetic induction simulated.

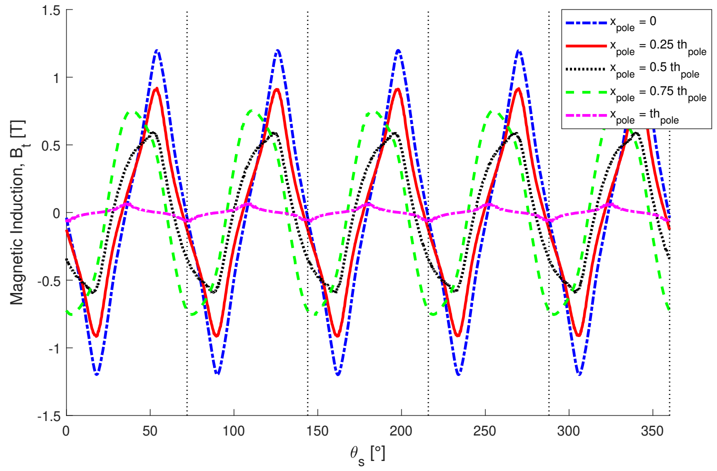

Figure 5.4: Tangential magnetic induction simulated.

5.2.4 Torque

The figure below represent the torque behavior resulting from a simulation under maximum torque conditions, as described at the beginning of this section. As it can be seen, the nominal torque on the sun side is about $T_{n-sun} = 2.57\ Nm$, this corresponds on a nominal torque of $T_{n-ring} = 2.57 \cdot 2.6 = 6.68\ Nm$ on the ring side. There is a small ripple due to the inevitable harmonics in the magnetic flux.

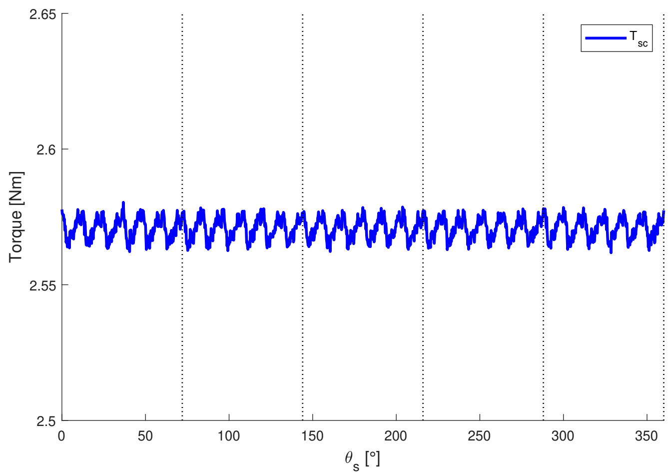

Figure 5.5: Nominal torque simulated on the sun side.

5.3 Experimental results at no-load

The experimental results were obtained with no-load tests. For emf, magnetic flux and magnetic induction measurements, the motor on the ring side was connected, while the one on the sun side was disconnected. For the torque measurements, on the other hand, no-load tests were carried out by first connecting the motor on the sun side and leaving the other one disconnected, and then doing the opposite, so connecting the motor from the ring side and disconnecting the one on the sun side. The tests were conducted at various speeds and for each of them the regime was expected to launch the acquisition.

For the measurements of emf, magnetic flux and magnetic induction there will be three graphs. This is because, as has been seen previously, the voltage measurements with the ocilloscope were made on the coils present on three ferromagnetic poles out of phase by 120 mechanical degrees.

5.3.1 Voltage

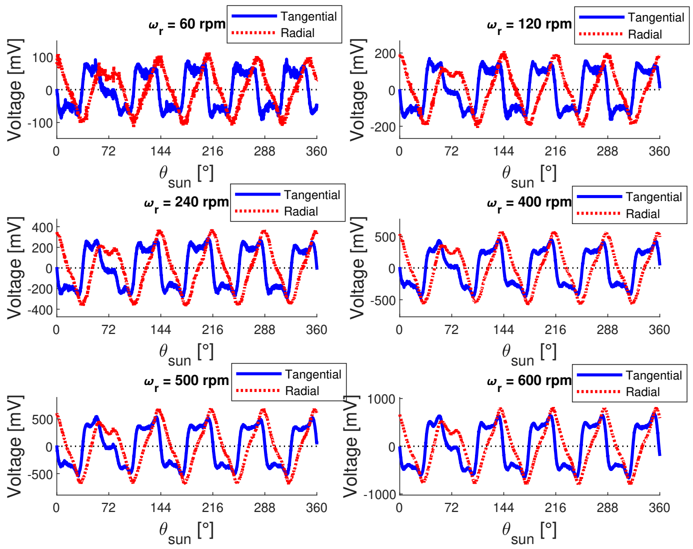

Figure 5.6: Voltage acquired from the coils of pole 1 versus sun rotation at different speeds.

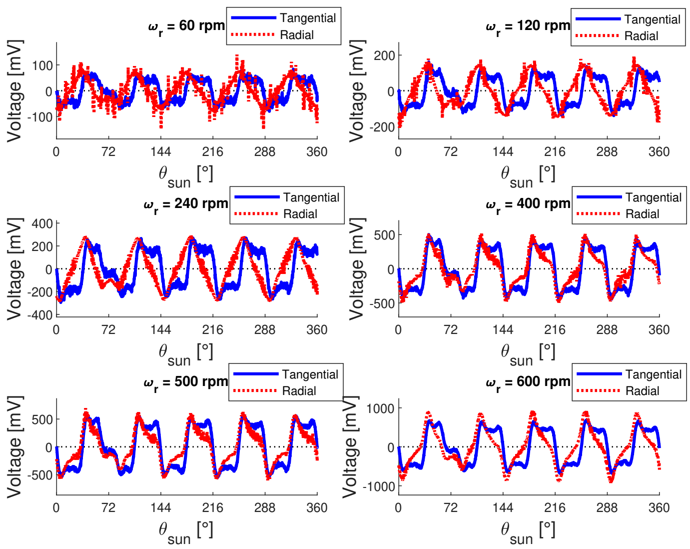

Figure 5.7: Voltage acquired from the coils of pole 2 versus sun rotation at different speeds.

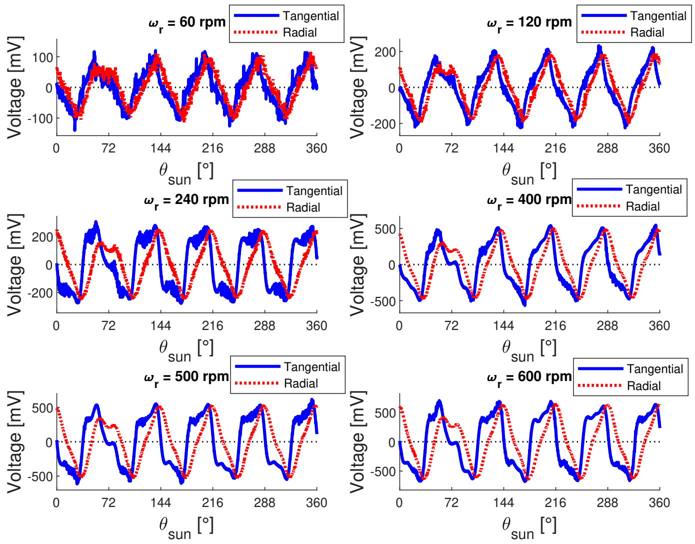

Figure 5.8: Voltage acquired from the coils of pole 3 versus sun rotation at different speeds.

5.3.2 Magnetic flux

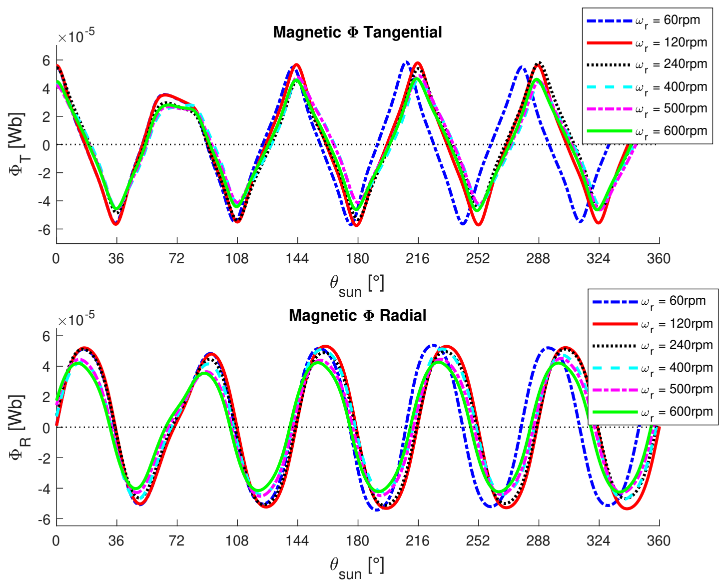

Figure 5.9: Tangential and radial magnetic flux using the voltage acquired from the coils of pole 1.

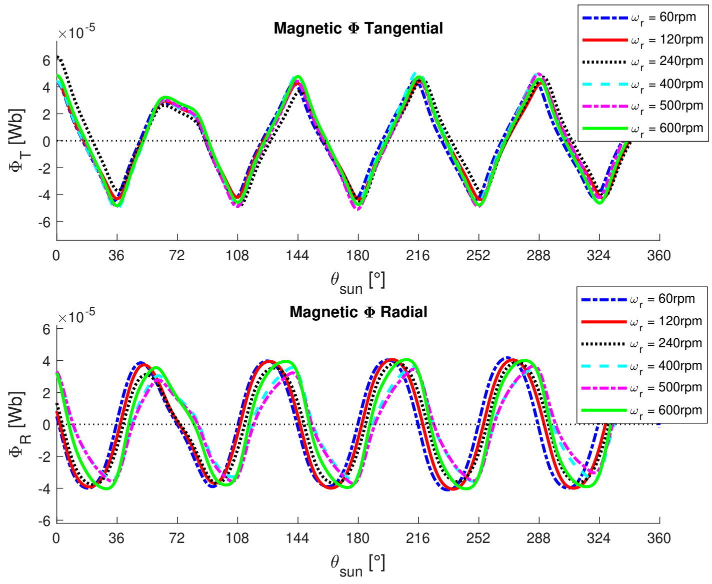

Figure 5.10: Tangential and radial magnetic flux using the voltage acquired from the coils of pole 2.

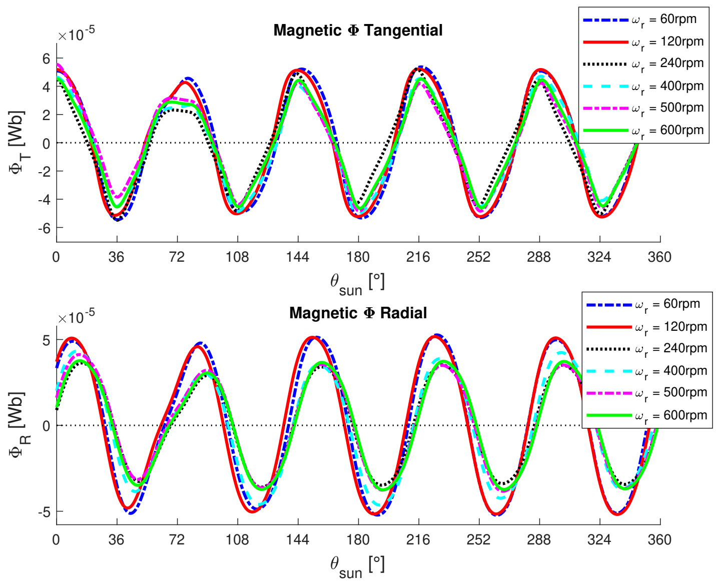

Figure 5.11: Tangential and radial magnetic flux using the voltage acquired from the coils of pole 3.

5.3.3 Magnetic induction

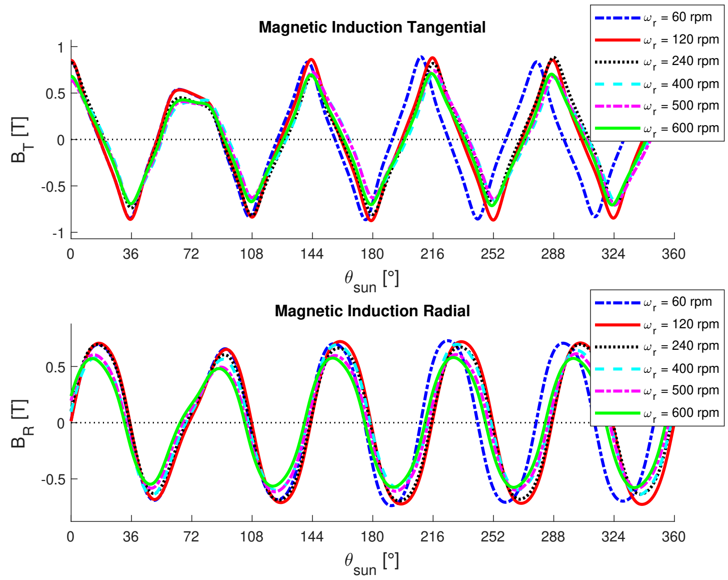

Figure 5.12: Tangential and radial magnetic induction using the voltage acquired from the coils of pole 1.

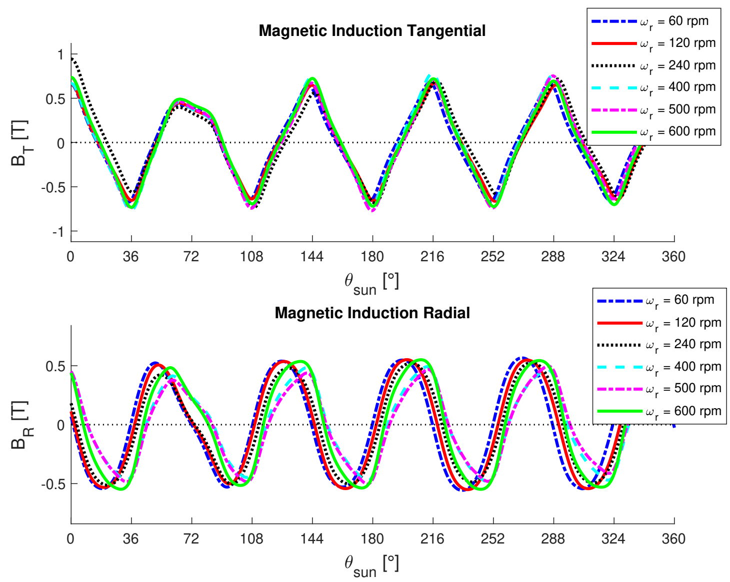

Figure 5.13: Tangential and radial magnetic induction using the voltage acquired from the coils of pole 2.

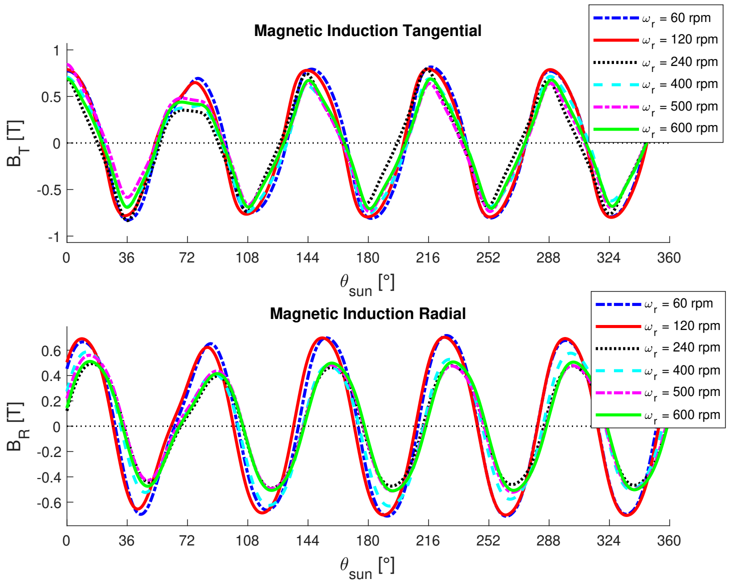

Figure 5.14: Tangential and radial magnetic induction using the voltage acquired from the coils of pole 3.

5.3.4 Torque

As these are no-load tests, the torque values acquired by the torque transducer will correspond to the losses of the magnetic gear. The torque transducer used to carry out the acquisitions is the one mounted on the shaft connected to the motor during the test. As previously mentioned, the tests were carried out by first connecting the motor on the ring side and then the one on the side of the sun. These tests were also carried out at different speeds and in particular, the reference speeds given to the two engines were calculated taking into account the gear ratio in order to make the results comparable. For example, during the no-load test with the motor connected on the ring side the reference speed given is $\omega_{ring} = 60rpm$, so when the opposite test is performed, connecting the motor on the sun side, the given speed will be $\omega_{sun} = 60 \cdot 2.6 = 156rpm$.

Ring side

Here is shown the figure representing the torque losses at different speeds. As it can be seen, as speeds increase, the torque losses increase. The waveforms obtained at low speeds are very similar, while those for high speeds have a larger ripple in amplitude and lower in frequency. At 660 rpm, the average lost torque is about 2.3 Nm, which corresponds to 34.4% of the nominal one of 6.68 Nm.

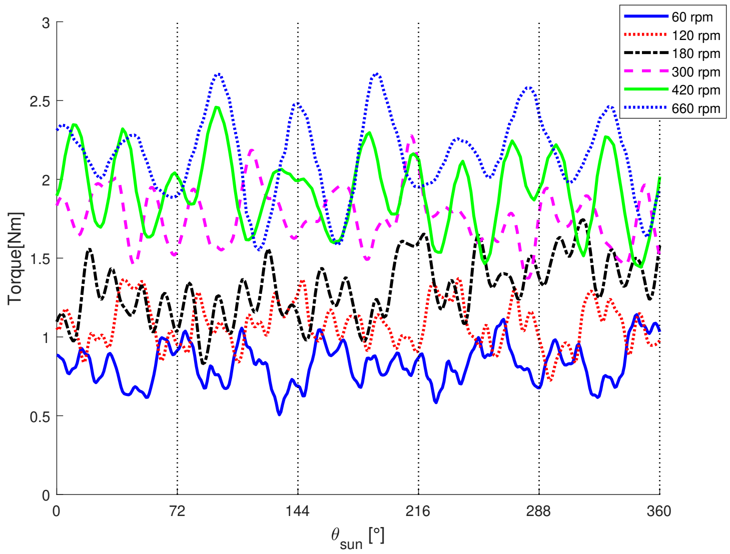

Figure 5.15: Torque losses at different speeds versus sun rotation (Ring side).

From the Fourier spectral analysis of the above waveforms it is possible to observe the presence of harmonics of an order equal to about 20 times that of the reference speed. For example, considering the blue line corresponding to the speed of 60 rpm, therefore 1 Hz, there is an harmonic at about 20 Hz.

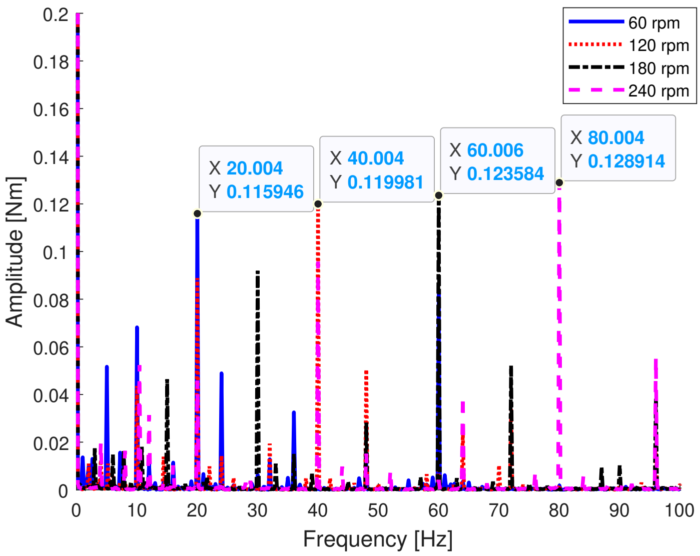

Figure 5.16: FFT (Fast Fourier Transform) of the torque losses at different speeds of the ring.

Figure 5.17 reports the measured values of the ring and sun speeds over time for a $w_{ring} = 60rpm$ in 5.17a and $w_{ring} = 360rpm$ in 5.17b, respectively. Moreover, having both speeds of the two shafts of the MG, it was possible to calculate and report the trend of the gear ratio. As can be seen, both the speeds and the gear ratio are subject to ripple. The mean value of the gear ratio corresponds exactly to the planned value of 2,6. It can be seen that the amplitude of the ripple decreases as the speed increases.

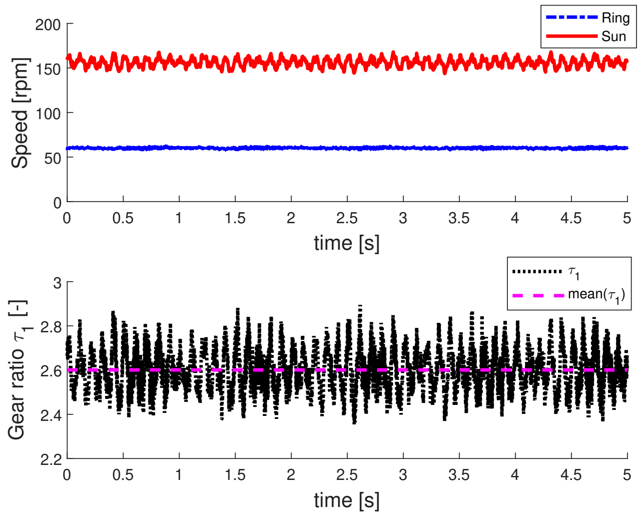

(a)

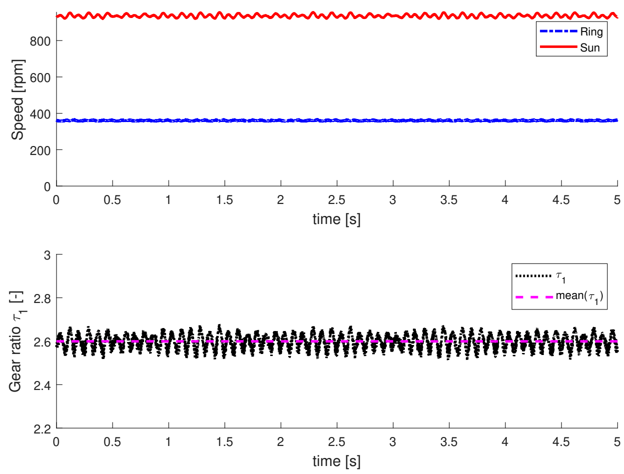

(b)

Figure 5.17: Speed and gear ratio ripple for $\omega_{ring} = 60rpm$(a) and $\omega_{ring} = 360rpm$(b).

The figure below shows the average torque values obtained at the different speeds. As it can be seen, in the graph there are three lines, this is because the values have been taken 3 times:

- Test 1: from zero up to the maximum speed of 660rpm.
- Test 2: form maximum speed to zero.
- Test 3: up again form zero to the maximum speed.

Tests 2 and 3 have lower lost torque values, this is probably due to the fact that the bearings have overheated and consequently the losses have decreased.

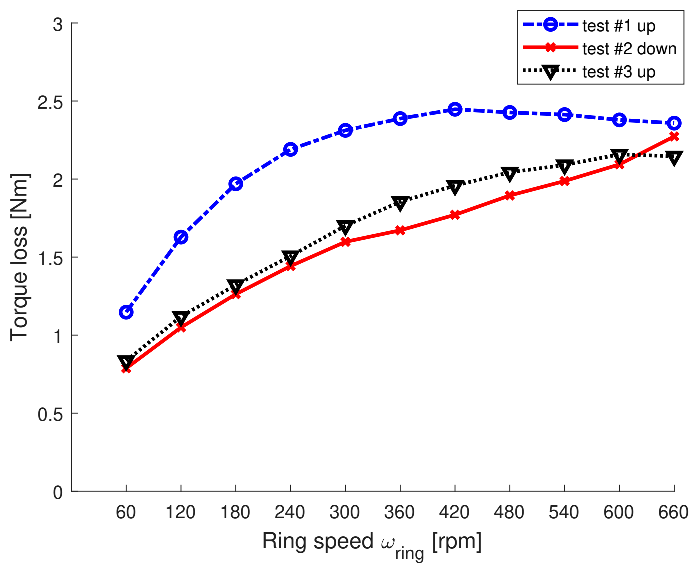

Figure 5.18: Mean value of torque losses at different speeds on three tests.

Sun side

As previously mentioned, the same torque tests were carried out by connecting the motor from the sun side, and here the dual results are reported.
From the following figure, comparing it with 5.15, it can be seen how the results obtained are different from each other, despite the fact that the rotation speeds of the two shafts have been kept the same in the two tests. Here, at 1482 rpm, the average lost torque is about 0.9 Nm which corresponds to 35.0% of the nominal one equal to 2.57 Nm.

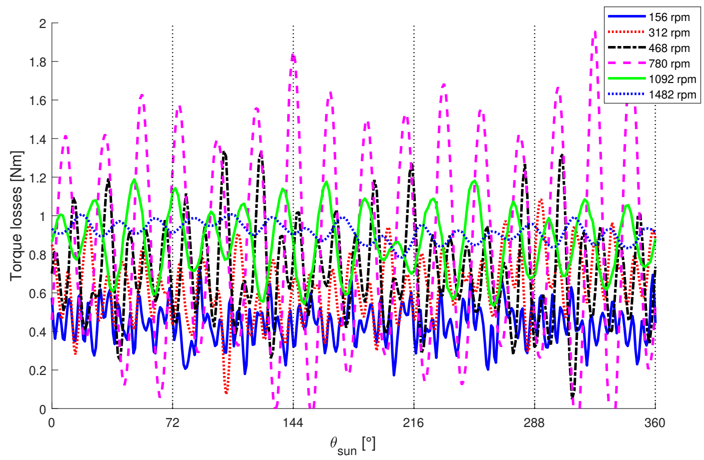

Figure 5.19: Torque losses at different speeds versus sun rotation (Sun side).

The Fourier spectral analysis allows us to note that also in this case there are harmonics related to the rotation speed. Also in this case the order of the harmonic is about 20 times with respect to the value of the speed set. For example, considering the red line corresponding to the speed of 312 rpm, therefore 5,2 Hz, there is an harmonic at about 104 Hz, which is 20 times bigger. Furthermore it can be noted that the order of the harmonics is 2.6 times (gear ratio) greater than those of figure 5.16 obtained from the test on the ring side.

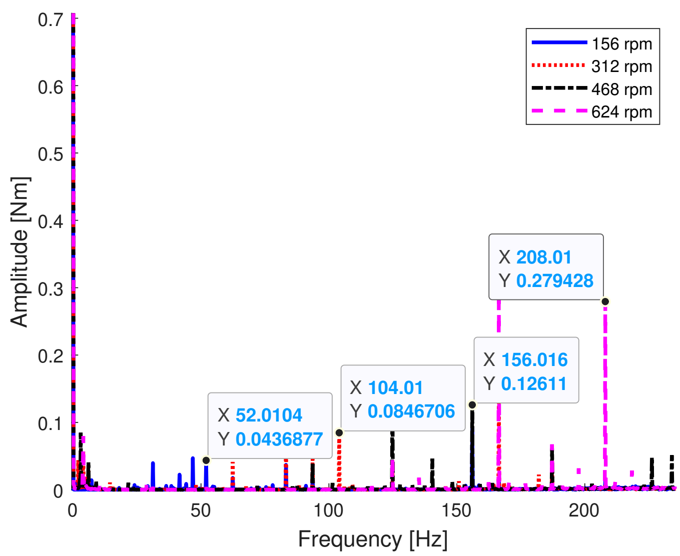

Figure 5.20: FFT (Fast Fourier Transform) of the torque losses at different speeds of the sun.

As done before the ripple is evaluated on speed and gear ratio. Here too it can be observed how the ripple decreases as the speed increases. Comparing the graph below with fig 5.17, however, it can be seen that in this case the ripple is very low, despite the fact that the test was carried out under the same conditions.

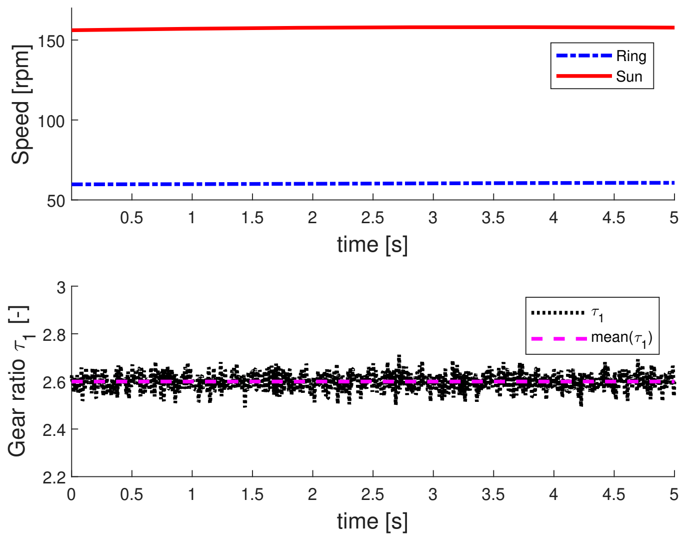

(a)

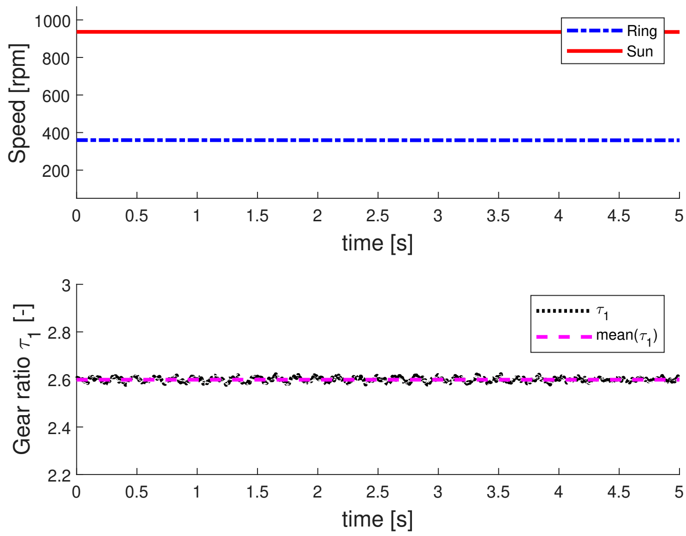

(b)

Figure 5.21: Speed and gear ratio ripple for $\omega_{sun} = 156rpm$(a) and $\omega_{sun} = 936rpm$(b).

Unlike what was done in the previous test, here the acquisitions were made during a single speed test from 0 to maximum speed.
The red line was obtained by multiplying the values of the blue line by the gear ratio, this was done in order to compare the lost torque trends with those obtained in the previous test. Furthermore, the data are represented as a function of the speed of the ring, again in order to be compared to those obtained from the test on the ring side.

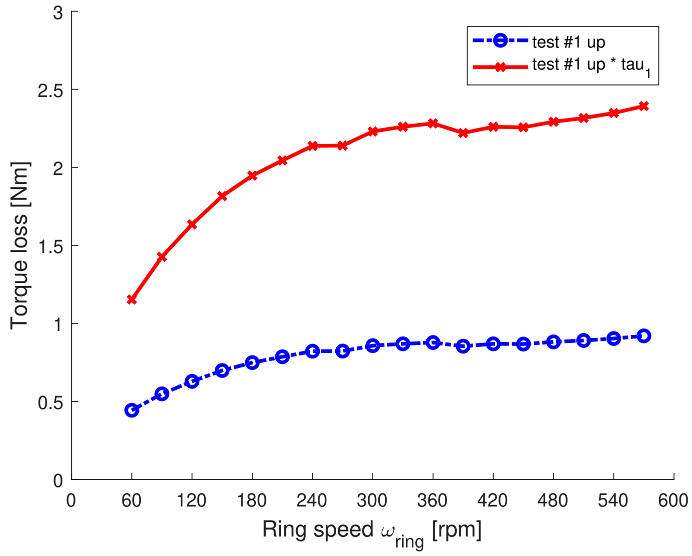

Figure 5.22: Mean value of torque losses for different speeds rotation of the sun.

5.4 Comparison

5.4.1 Magnetic flux

The figures below show the comparison between the simulated and measured radial and tangential magnetic flux. To make the comparison with the simulated waveform, the one measured by the third pole at a speed of $\omega_{ring} = 60rpm$ was taken. As it can be seen, the waveforms are very similar, even if their amplitude is not exactly the same.

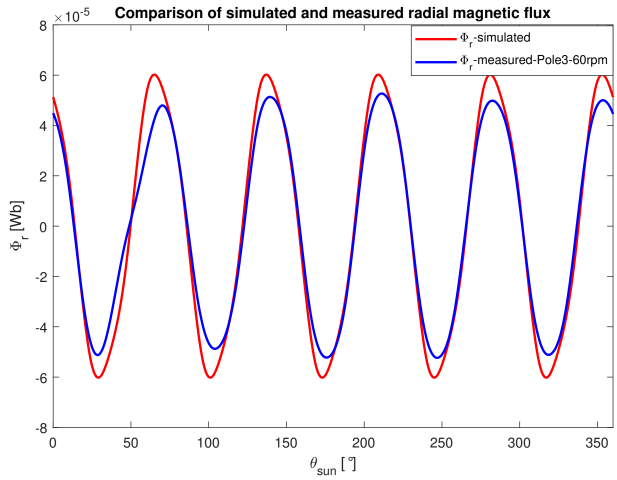

Figure 5.23: Comparison of simulated and measured radial magnetic flux.

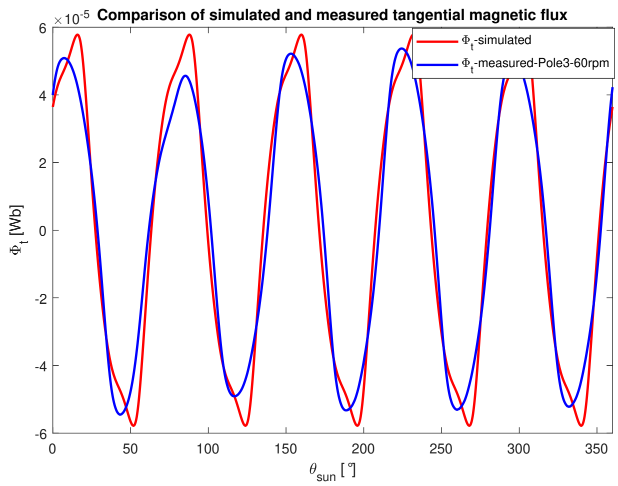

Figure 5.24: Comparison of simulated and measured tangential magnetic flux.

5.4.2 Magnetic induction

For the comparison of the radial and tangential magnetic induction, the simulated waveform corresponding to the point $x_{pole} = 0.5$ of the ferromagnetic pole was used, while for the one measured the one measured by the third pole at a speed of $\omega_{ring} = 60rpm$ was used. Similarly to the comparison of the fluxes it is observed how the waveforms are similar while their amplitude does not coincide perfectly.

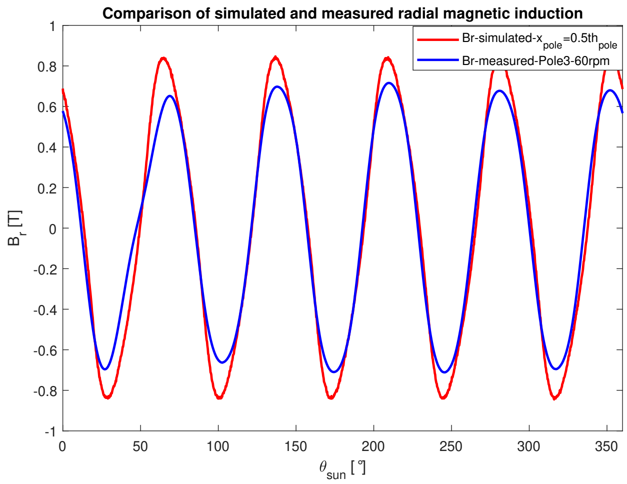

Figure 5.25: Comparison of simulated and measured radial magnetic induction.

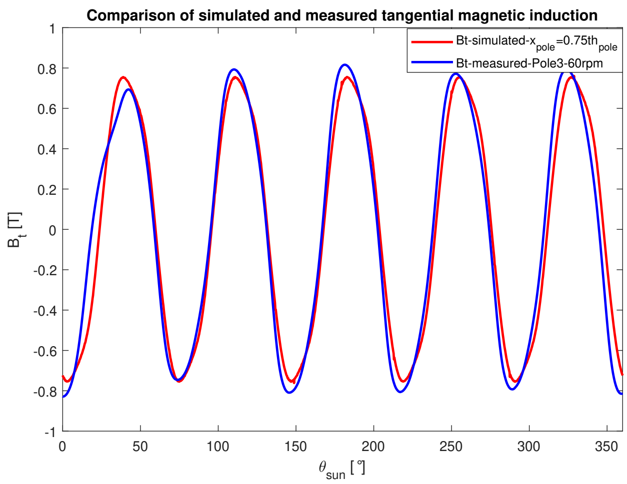

Figure 5.26: Comparison of simulated and measured tangential magnetic induction.

5.4.3 Torque and power losses

As can be seen from the figure below, the torque tests carried out on the sun side and the ring side provide very similar average values of torque loss. In this case, the first test of the three carried out on the ring side was compared with that on the sun side because, as it is recalled, it is the only test that was carried out for the sun side. It can be thought that by carrying out three tests on the sun side, the lost torque values could have decreased, as in the case of the other test.

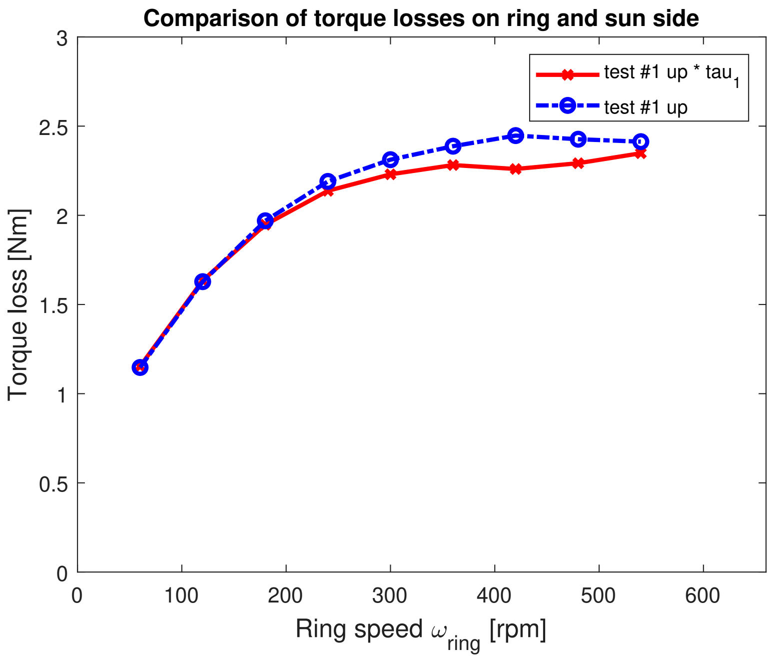

Figure 5.27: Comparison of torque losses on ring and sun side tests.

The values of power loss reported below have been obtained by multiplying those of lost torque by the corresponding speed. It is observed how the link between the power loss and the speed is of a linear type and how the values reached by the power are quite high.

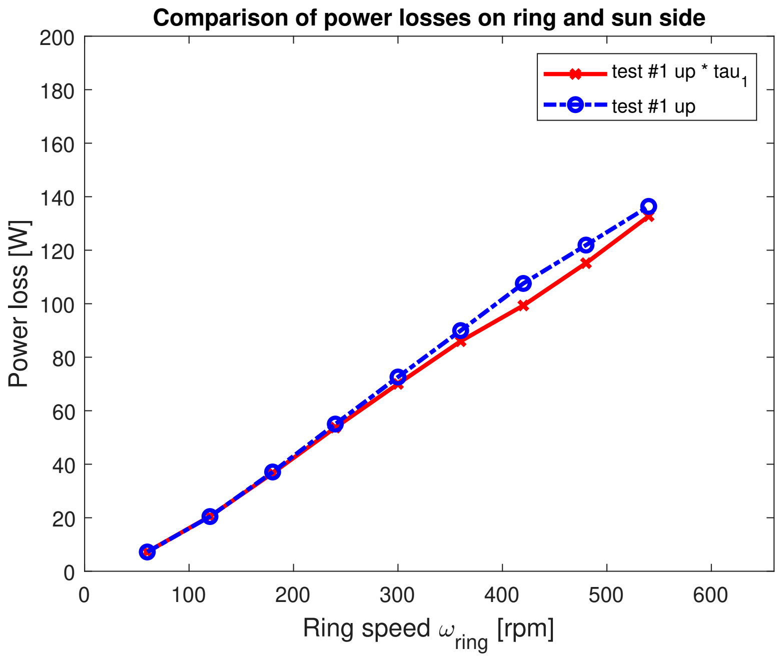

Figure 5.28: Comparison of power losses on ring and sun side.

5.5 Comments on the results obtained

Analyzing the graphs obtained experimentally it will surely be noticed that the waveforms of magnetic fluxes and magnetic induction have an anomaly of the second wave, in fact the latter has a shape and amplitude different from the others. This anomaly can also be found in the electromotive force graphs. The prototype was then sent for repair to be checked. The problem that was detected by the experimental measurements was due to an incorrect positioning of the magnets on the sun. As can be seen from figure 5.29a, the magnets that make up the pole pair are actually made up of 6 magnets attached to each other. In figure 5.29b it can be seen instead the real positioning of the magnets inside the prototype on a pole pair of the sun. Two magnets were reversed and gave rise to the anomaly found in the graphs.This error was present on a single polar pair of the sun.
It was not possible to carry out a simulation to verify if the problem was due to the inversion of the magnets before sending the prototype for repair as the FEMM software allows the simulation in 2D, thus making it impossible to represent the real configuration of the magnets as they are positioned on two rows.

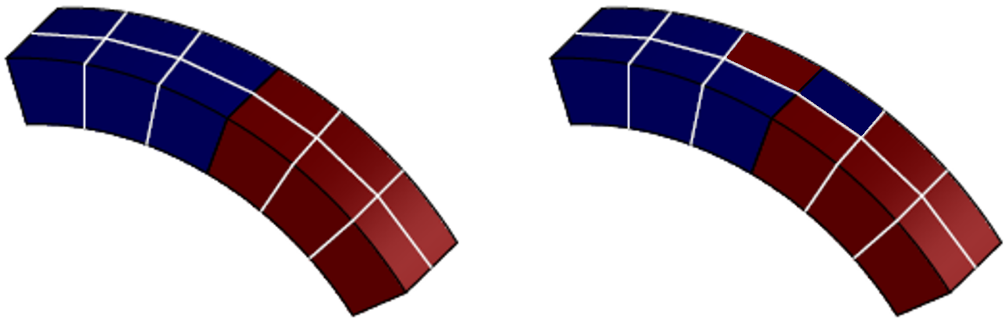

(a) (b)

Figure 5.29: Theoretical composition of the pole pair of the sun (a) and real wrong composition of the prototype (b) (only 1 polar pair was incorrectly assembled).

The prototype also made a sliding noise during testing. Once sent for repair it was confirmed that the bearings had suffered damage and were not working well. This problem has probably partially compromised the tests carried out and justifies the high values of torque and power loss, equal to about 35% of the nominal values as seen above.

Chapter 6

Conclusion

The results obtained from the experimental no-load tests presented in chapter 5.2 allow a first characterization of the prototype. As has been discussed and as seen from the comparisons, the results obtained reflect those expected from the simulations. This confirms how the test bench is able to perform the role for which it was designed and how the prototype is actually able to transfer torque according to the simulations and analyzes made during the design phase.
When the prototype is adjusted, the tests presented in this thesis will be repeated and new ones will be carried out in order to continue to characterize the magnetic gear.
In particular, overload tests will be carried out as well as tests to measure the efficiency of the magnetic gear, which were foreseen for this thesis activity, but which were not made due to the inconvenience of the breakage of the MG.
As regards the test for measuring the efficiency of the MG, both motors will be connected and tests will be carried out at different speeds and with different load torque values. By measuring the torque and speed values at the extremes of the MG using the encoders and the torque transducers, the input and output powers are calculated and therefore the efficiencies. The expected result is a map with the efficiency values obtained as a function of speeds and load torques. This test will be carried out twice, considering first one motor as a driving force and the other as a load and subsequently reversing their roles, so as to be able to compare the efficiency values obtained in the two cases.
All these experimental activities will allow to understand the real potential of the magnetic gear.

Appendix A

Appendix of Hardware chapter

A.1 Unifilar scheme

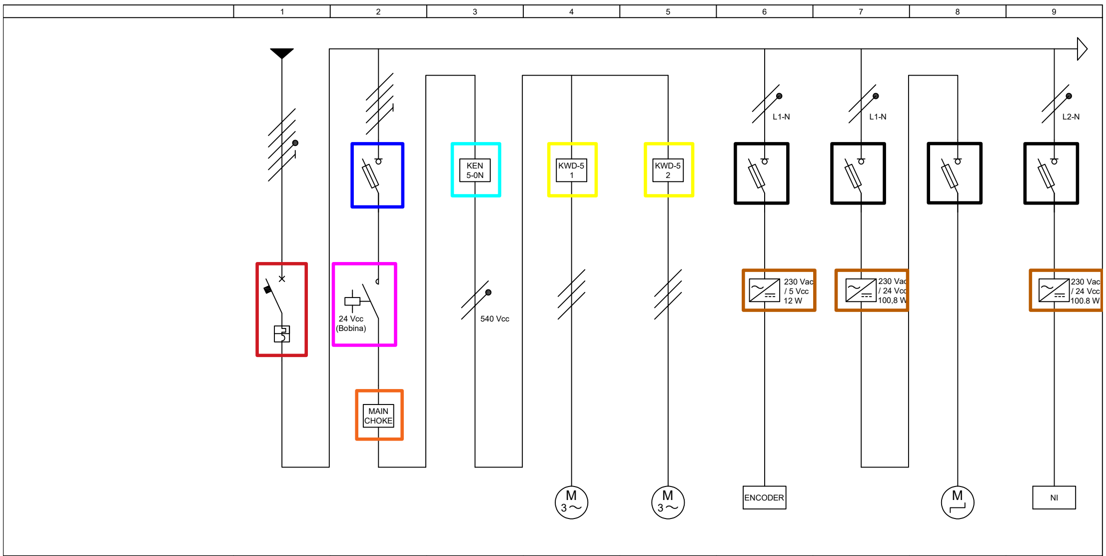

NUMERAZIONE CIRCUITO		1	2	3	4	5	6	7	8	9
DENOMINAZIONE		MAGNETOTERM. GENERALE	PROTEZIONE CONVERTITORE	RADDRIZZATORE KEN 5-0N	INVERTER KWD-5 + MOTORE 1	INVERTER KWD-5 + MOTORE 2	ENCODER	INTERRUTTORE SEZIONATORE FUSIBILE	MOTORE STEPPER	SCHEDA NATIONAL INSTRUMENT
TENSIONE		400	400	540 cc			5 cc	230	24 cc	24 cc
PROTEZIONE	TIPO	MODULARE	MODULARE				MODULARE	MODULARE	MODULARE	MODULARE
	POLI	4P	3P				2P	2P	2P	2P
	I nominale [A]	16	16				1	1	2	1
	P.d.i. [kA]	10	160				120	120	120	120
	Curva	C	gR				gL	gL	gL	gL
UTENZE	P nominale [W]			5000	5000	5000			48	
	I nominale [A]			9.25			0,035		2	4,2
LINEA	TIPO POSA	QUADRO	QUADRO	QUADRO	CAVO	CAVO	CAVO	QUADRO	CAVO	QUADRO
	Sez. [mm2]	4x2,5 + PE	3x2,5 + PE				2x1,5	2x1,5	2x1,5	2x1,5

IMPIANTO: Quadro elettrico per banco di prova

PROGETTISTA: Gabriele Pirra, Nicola La Bella

DATA: 29/11/2020

PAGINA 1 di 2

Figure A.1: Unifilar scheme 1/2

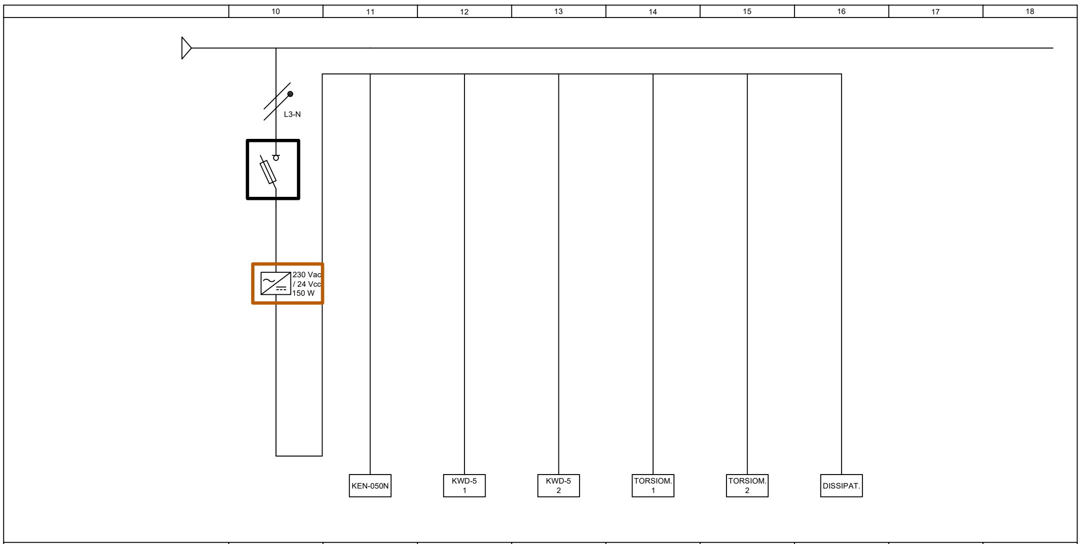

NUMERAZIONE CIRCUITO		10	11	12	13	14	15	16	17	18
DENOMINAZIONE		INTERRUTTORE SEZIONATORE FUSIBILE	RADDRIZZATORE KEN 5-0N Aliment. 24Vcc	INVERTER KWD-5 (1) Aliment. 24Vcc	INVERTER KWD-5 (2) Aliment. 24Vcc	TORSIOMETRO 1	TORSIOMETRO 2	DISSIPATORE CALORE CONVERTITORE		
TENSIONE		230	24 cc	24 cc	24 cc	24 cc	24 cc	24 cc		
PROTEZIONE	TIPO	MODULARE								
	POLI	2P								
	I nominale [A]	1								
	P.d.i. [kA]	120								
	Curva	gL								
UTENZE	P nominale [W]		5	24	24	12	12			
	I nominale [A]		0,2	1	1	0,5	0,5			
LINEA	TIPO POSA	QUADRO	QUADRO	QUADRO	QUADRO	CAVO	CAVO	QUADRO		
	Sez. [mm2]	2x1,5	2x1,5	2x1,5	2x1,5	2x1,5	2x1,5	2x1,5		

IMPIANTO: Quadro elettrico per banco di prova	PROGETTISTA: Gabriele Pirra, Nicola La Bella	DATA: 29/11/2020
		PAGINA 2 di 2

Figure A.2: Unifilar scheme 2/2

A.2 Electrical panel

Figure A.3: Electrical panel

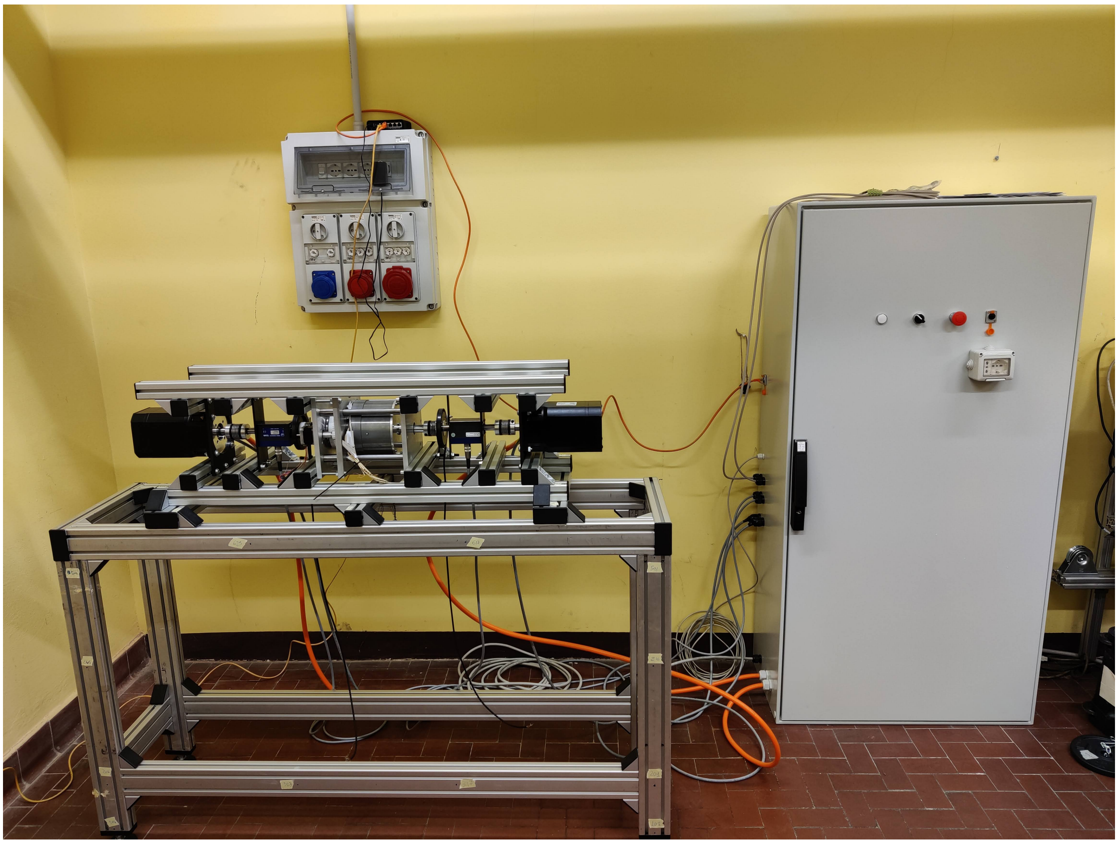

Figure A.4: Overview of the complete test bench.

A.3 Electic drive

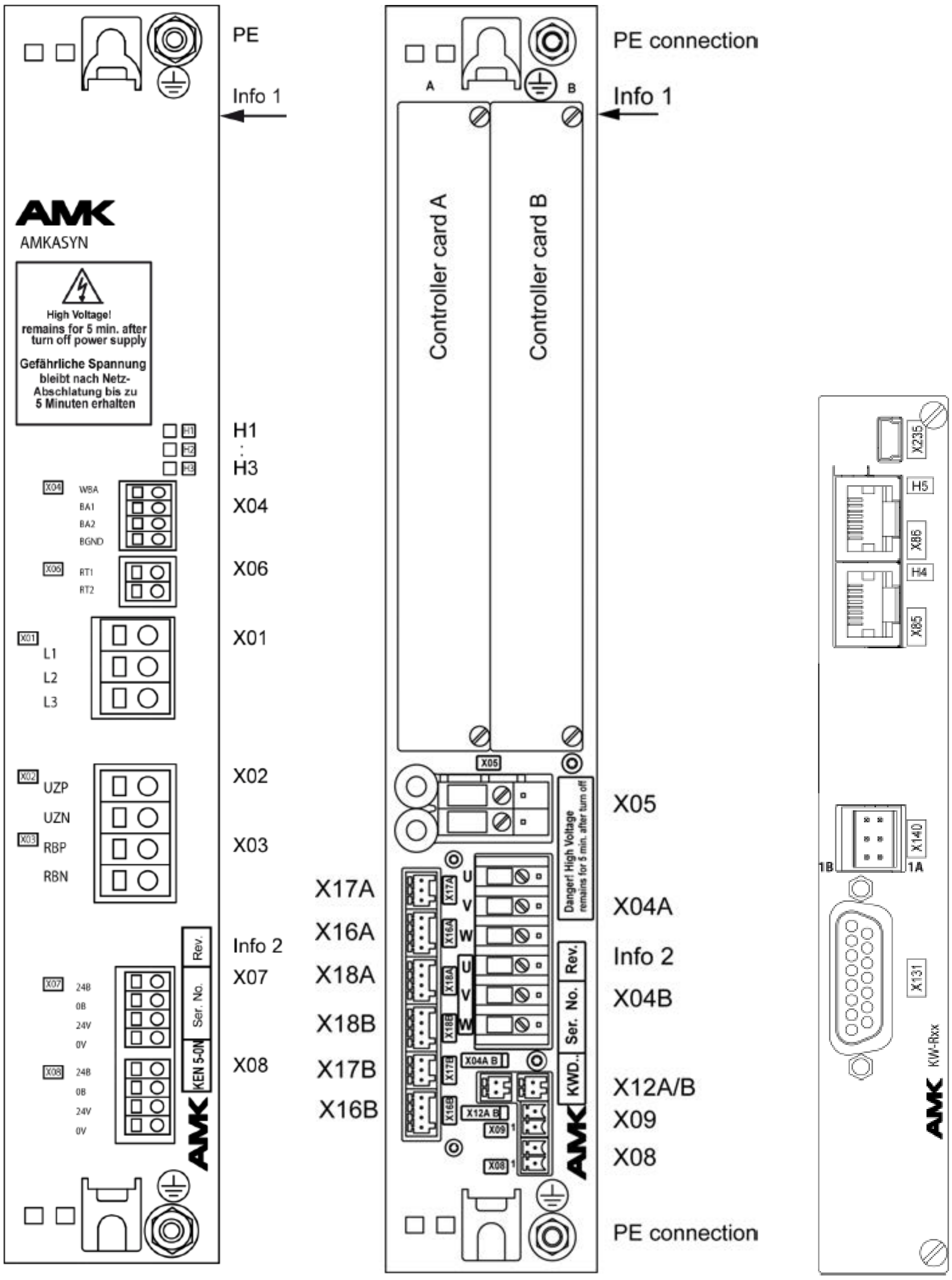

(a) (b) (c)

Figure A.5: Modules for Controller cRIO [16]: (a) KEN 5-0N, (b) KWD5, (c) r25 controller card.

Interfaces	Function
H1/H2/H3	LED status indicator
L1/L2/L3 [X01]	Power supply
UZP [X02]	DC bus voltage (+)
UZN [X02]	DC bus voltage (-)
RBP [X03]	Connection for external brake resistor
RBN [X03]	Connection for external brake resistor
RT1 [X06]	Connection PTC thermistor
RT2 [X06]	Connection PTC thermistor
24V [X08]	Connection 24 VDC logic supply input
0V [X08]	Connection 0 VDC logic supply input
24V [X07]	Connection 24 VDC logic supply output
0V [X07]	Connection 0 VDC logic supply output

Table A.1: KEN 5-0N Pins [16].

Interfaces	Function
X05	DC bus voltage
X04A	Motor 1 power supply connection
X04B	Motor 2 power supply connection
X12A/B	Temperature sensor motor PTc thermistor
X08	Connection 24 VDC logic supply
X16A/B	Power output stage enable
X17A/B	Power output stage enable
X18A/B	Power output stage enable

Table A.2: KWD5 Pins [16].

Interfaces	Function
H2-H5	Status LEDs
X86	Real-time Ethernet OUT
X85	Real-time Ethernet IN
X131	Sine encoder input

Table A.3: r25 controller card Pins [17].

Appendix B

Appendix of Software chapter

B.1 NI DAQmx main blocks

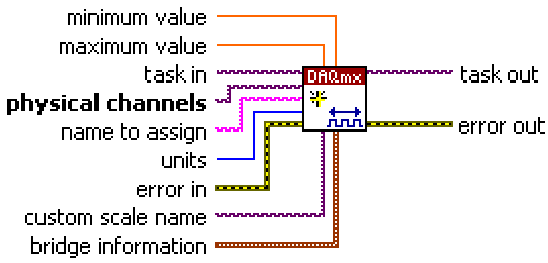

Figure B.1: NI DAQmx Create Virtual Channel block [18].

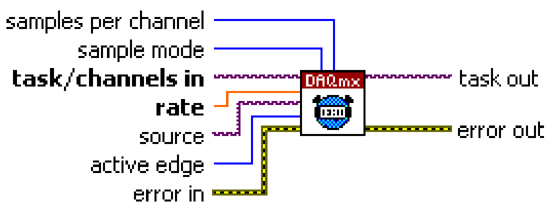

Figure B.2: NI DAQmx Timing block [18].

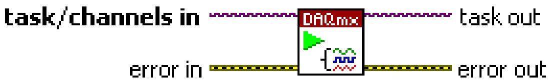

Figure B.3: NI DAQmx Start Task block [18].

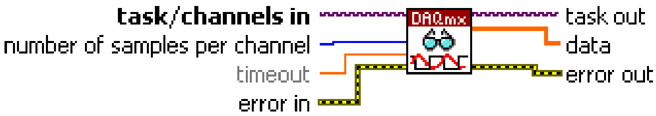

Figure B.4: NI DAQmx Read block [18].

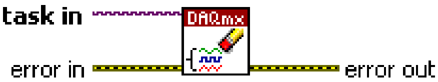

Figure B.5: NI DAQmx Clear Task block [18].

Bibliography

[1] K.Atallah and D. Howe. «A Novel high-performance magnetic gear for transmission mechanism». In: (2001), pp. 2844–2846 (cit. on pp. 1, 2, 6).

[2] Yawei Wang, Mattia Filippini, Nicola Bianchi, and Piergiorgio Alotto. «A Review on Magnetic Gears: Topologies, Computational Models and Design Aspects». In: (2019) (cit. on p. 2).

[3] C. Armstrong. «Power-transmitting device». US Patent 687,292. Nov. 1901 (cit. on p. 2).

[4] H. Faus. «Magnet gearing». US Patent 2,243,555. May 1941 (cit. on p. 2).

[5] Candidate: Raphael BARNOUIN - Supervisor: Giancarlo GENTA. «Thesis : Magnetic gears - description and applications for car industry (Politecnico di Torino)». In: (2016) (cit. on pp. 2, 4).

[6] T. B. Martin Jr. «Magnetic transmission». US Patent 3,378,710. Apr. 1968 (cit. on p. 2).

[7] Raouf Benlamine, Tahar Hamiti, Franck Vangraefschèpe, Frédéric Dubas, and Dominique Lhotellier. *Modeling of a Coaxial Magnetic Gear Equipped with Surface Mounted PMs Using Nonlinear Adaptive Magnetic Equivalent Circuits*. 2019. URL: `https://hal.archives-ouvertes.fr/hal-02130956/document` (cit. on p. 3).

[8] Engineering Insider. *What Is A Magnetic Gear and How It Works!* 2021. URL: `https://engineeringinsider.org/magnetic-gear-working/4/` (cit. on p. 3).

[9] Melaine Desvaux, Bernard Multon, Hamid Ben Ahmed, Stéphane Sire, Roman Le Goff Latimier, and Benjamin Traullé. *Computation Time Analysis of the Magnetic Gear Analytical Model*. 2017. URL: `https://hal.archives-ouvertes.fr/hal-01598128/document` (cit. on p. 4).

[10] Yawei Wang, Mattia Filippini, Giacomo Bacco, and Nicola Bianchi. «Parametric Design and Optimization of Magnetic Gears with Differential Evolution Method». In: (2018) (cit. on p. 5).

[11] Mattia Filippini, Piergiorgio Alotto, Vincenzo Cirimele, Maurizio Repetto, Carlo Ragusa, Luca Dimauro, and Elvio Bonisoli. «Magnetic Loss Analysis in Coaxial Magnetic Gears». In: (2019) (cit. on pp. 7–11).

[12] Vincenzo Cirimele, Maurizio Repetto, Luca Dimauro, and Elvio Bonisoli. «Multi-objective Optimisation of a Magnetic Gear for Powertrain Applications». In: (2020) (cit. on pp. 12, 13).

[13] *Servomotori Brushless - Serie SVTM A (Datasheet)*. Rev. 2.3. Servotecnica S.p.A. May 2019 (cit. on p. 17).

[14] *Torque transducer HBM T21WN (Datasheet)*. HBM (cit. on p. 19).

[15] *LM10 incremental magnetic encoder system (Datasheet)*. Rev. 15. RLS. May 2018 (cit. on pp. 20, 37, 38).

[16] *PDK 028932 KEKW Hardware en (Datasheet)*. AMK. 2019 (cit. on pp. 29, 30, 76, 77).

[17] *PDK 204918 KW-R2x (Datasheet)*. AMK. 2020 (cit. on p. 77).

[18] «LabVIEW help web site». In: (2018) (cit. on pp. 78, 79).